## AFRL-SN-WP-TR-2004-1054

# LASER INDUCED DESORPTION TIME OF FLIGHT MASS SPECTROMETER ANALYSIS OF ADSORBED CONTAMINANTS ON VACUUM ULTRAVIOLET LITHOGRAPHY OPTIC MATERIALS

**Dr. Susan D. Allen**
**Yamini Surpaneni**

**Florida State University**
**118 N. Woodward Avenue**
**Tallahassee, FL 32306-4166**

**FEBRUARY 2004**

**Final Report for 01 August 2000 – 01 December 2003**

**STINFO FINAL REPORT**

**SENSORS DIRECTORATE**
**AIR FORCE RESEARCH LABORATORY**
**AIR FORCE MATERIEL COMMAND**
**WRIGHT-PATTERSON AIR FORCE BASE, OH 45433-7320**

# NOTICE

THIS TECHNICAL REPORT HAS BEEN REVIEWED AND IS APPROVED FOR PUBLICATION.

/s/

GLEN D. VIA, Project Engineer
Electron Devices Branch
Aerospace Components Division

/s/

KENICHI NAKANO, Chief
Electron Devices Branch
Aerospace Components Division

/s/

ALAN J. TEWKSBURY, Acting Chief
Aerospace Components Division
Sensors Directorate

| REPORT DOCUMENTATION PAGE | *Form Approved*<br>*OMB No. 0704-0188* |
|---|---|

**1. REPORT DATE** ***(DD-MM-YY)***
February 2004

**2. REPORT TYPE**
Final

**3. DATES COVERED** ***(From - To)***
08/01/2000 – 12/01/2003

**4. TITLE AND SUBTITLE**
LASER INDUCED DESORPTION TIME OF FLIGHT MASS SPECTROMETER ANALYSIS OF ADSORBED CONTAMINANTS ON VACUUM ULTRAVIOLET LITHOGRAPHY OPTIC MATERIALS

**5a. CONTRACT NUMBER**
F33615-00-1-1727

**5b. GRANT NUMBER**

**5c. PROGRAM ELEMENT NUMBER**
69199F

**6. AUTHOR(S)**
Dr. Susan D. Allen
Yamini Surpaneni

**5d. PROJECT NUMBER**
ARPS

**5e. TASK NUMBER**
ND

**5f. WORK UNIT NUMBER**
0V

**7. PERFORMING ORGANIZATION NAME(S) AND ADDRESS(ES)**

Florida State University
118 N. Woodward Avenue
Tallahassee, FL 32306-4166

**8. PERFORMING ORGANIZATION REPORT NUMBER**

**9. SPONSORING/MONITORING AGENCY NAME(S) AND ADDRESS(ES)**

Sensors Directorate
Air Force Research Laboratory
Air Force Materiel Command
Wright-Patterson AFB, OH 45433-7320

**10. SPONSORING/MONITORING AGENCY ACRONYM(S)**
AFRL/SNDD

**11. SPONSORING/MONITORING AGENCY REPORT NUMBER(S)**
AFRL-SN-WP-TR-2004-1054

**12. DISTRIBUTION/AVAILABILITY STATEMENT**
Approved for public release; distribution is unlimited.

**13. SUPPLEMENTARY NOTES**
Report contains color. This report is a thesis submitted to the Department of Electrical and Computer Engineering in partial fulfillment of the requirements for the degree of Master of Science.

**14. ABSTRACT**

Adsorbed surface contaminants on optical elements absorb light energy in an optical lithography system and, if left unclean, will result in reduced wafer yield. In order to nondestructively analyze the surface adsorbate of different CaF2 samples, a laser induced desorption-Time of Flight Mass Spectrometer (LID-TOFMS) technique was developed. The main object of this technique is to investigate the surface composition of adsorbed contaminants as a function of position on the sample. An Er:YAG laser at 2.94 μm was used as the light source to induce desorption. Electron impact ionization was used to obtain ionization of desorbed molecules. The detection of ionized species was accomplished by TOFMS operated in Angular Reflectron (AREF) mode to obtain better resolution.

The data reported here can be used in semiconductor industries either to modify conventional processing or to design a new efficient laser cleaning process for optical elements.

**15. SUBJECT TERMS**
Optics, Laser Application, Electronic Products and Processes

| 16. SECURITY CLASSIFICATION OF: | | | 17. LIMITATION OF ABSTRACT: | 18. NUMBER OF PAGES | 19a. NAME OF RESPONSIBLE PERSON (Monitor) |
|---|---|---|---|---|---|
| a. REPORT | b. ABSTRACT | c. THIS PAGE | | | Glen D. Via |
| Unclassified | Unclassified | Unclassified | SAR | 108 | 19b. TELEPHONE NUMBER *(Include Area Code)*<br>(937) 255-1874 x3457 |

# TABLE OF CONTENTS

# LIST OF FIGURES

# LIST OF TABLES

# ABSTRACT

The semiconductor industry currently uses optical lithography processes at the 130 nm node (90 nm gate length) for fabricating integrated circuits (ICs). This lithography process uses a 248nm wavelength light source to write features on wafers. The next generation of integrated chips is slated to be fabricated at a 90 nm node using 193 nm wavelength light source. 193 nm lithography tools that have already met International SEMATECH (ISMT) standards are ready for use in mass production of ICs. In the next next generation, 157nm is the candidate optical lithography tool to produce ICs at the 70 nm node. The optical elements that are being used in stepper tools until now are highly absorptive at 157nm. Calcium fluoride ($CaF_2$) is the material of choice for optical elements at 157nm due to its high transmittance in the deep ultraviolet (DUV) and vacuum ultraviolet (VUV) spectral ranges.

Adsorbed surface contaminants on optical elements absorb light energy in an optical lithography system and, if left unclean, will result in reduced wafer yield. In order to nondestructively analyze the surface adsorbate of different $CaF_2$ samples, a laser induced desorption - Time of Flight Mass Spectrometer (LID-TOFMS) technique was developed. The main object of this technique is to investigate the surface composition of adsorbed contaminants as a function of position on the sample. An Er:YAG laser at 2.94µm was used as the light source to induce desorption. Electron impact ionization was used to obtain ionization of desorbed molecules. The detection

of ionized species was accomplished by TOFMS operated in Angular Reflectron (AREF) mode to obtain better resolution.

Super polished, (100) $CaF_2$ and different off-axis (such as $10^{\circ}$ and $15^{\circ}$ off (100)) $CaF_2$ samples were investigated in this work. Water, alcohols, ketones and alkali metal ions were found on all the samples. Water ions and hydrocarbon ions (from alcohols and ketones) were seen at most of the sites while alkali metal ions were less frequently observed. A degenerate desorption threshold model was used to quantitatively analyze the desorbed species and to determine desorption threshold energy density at numerous sites on all the samples. Surface maps of water ions and hydrocarbon ions for different samples were plotted and they showed similar distribution patterns of water and hydrocarbon ions on the sample surface. This suggests that water and hydrocarbons are co-adsorbed or incorporated into surface defects during the polishing and cleaning operations. Atomic force microscope (AFM) scans of the samples were performed to identify surface topography.

The data reported here can be used in semiconductor industries either to modify conventional processing or to design a new efficient laser cleaning process for optical elements.

# CHAPTER 1

# INTRODUCTION

Continuous advances are being pursued in the miniaturization of features written on silicon wafer in order to improve device performance in integrated circuits (ICs). As the feature size decreases, speed of the devices increases due to smaller gate lengths. Semiconductor industries are currently using 300mm silicon wafers. With silicon wafer diameter remaining constant, reduction in minimum feature size allows for adding more and more transistors, thus resulting in the development of more complex circuitry on a single chip. This results in reduced cost of ICs.

The minimum feature size that can be printed by an optical lithography technology is limited by its resolution. According to Rayleigh's resolution criterion, resolution of a lithography system can be obtained by using equation 1.1 where $k_1$ represents Rayleigh's constant (a measure of contrast in the exposed image), $\lambda$ represents the wavelength of the light source and NA represents the numerical aperture (a measure of ability of lens to collect light) of the lens system used in lithography process.

$$R = k_1 * (\lambda/NA) \qquad 1.1.$$

Therefore, increased resolution can be obtained by either decreasing wavelength or increasing NA. Increasing NA results in a smaller depth of focus (depth of focus is inversely proportional to square of NA). In a lithography process various layers such as insulating oxide and metal etc. are laid on wafer surface. These layers add hills and valleys to the wafer's surface and the chip's image is projected onto an uneven surface. Thus, a higher NA means degraded image, resulting in reduced wafer yields. Moreover, higher NA lenses are larger and, therefore, expensive. For conventional optical lithography processes, the minimum value of the $k_1$ factor is 0.5, limited again by image quality degradation.[1] Also, changing $k_1$ factor can bring support to an existing technology and can not produce an efficient new lithography technology.[2] Hence, the other factor – wavelength – is normally changed to achieve improved resolution.

The different exposure wavelength bands used in optical lithography are given in Table 1.1. The UV range is subdivided into two ranges: deep ultraviolet (DUV) and vacuum ultraviolet (VUV). (Note that 157 nm is not technically VUV, although it is traditionally referred to as such. High purity $N_2$ is transparent at 157 nm and the developing lithographic systems at this wavelength are being designed for use with a high purity $N_2$ purge. Recent lithographic literature frequently refers to 157 nm as DUV).

Table 1.1. Wavelength bands

| Wavelength (nm) | Name | Sub range (nm) | Name |
|---|---|---|---|
| 380 – 780 | Visible | | |
| 100 – 380 | UV | 190 – 280 | DUV |
| | | 100 – 190 | VUV |
| 5 – 100 | EUV | | |

Different wavelength ranges require different lithography technologies. In other words, lithography technologies using visible, ultraviolet (UV) and extreme ultraviolet (EUV) wavelengths are different, as different exposure equipment, photoresists and process controls are required at different wavelengths.

Lithography technologies down to the 800 nm node used the blue mercury line (g-line) at 435.83 nm and ultraviolet mercury line (i-line) at 365.01 nm as light sources to produce ICs. The transition from i/g line steppers to DUV (≤ 248 nm) made possible the sub wavelength patterning. Table 1.2 shows the different wavelengths used to produce integrated circuits at different nodes (minimum feature sizes). It also gives the year in which different technologies are/expected to be introduced and the number of transistors per IC along with the name of the processor manufactured using the technologies. An interesting fact is that the number of transistors in a single chip is increasing exponentially – almost doubling every eighteen months as G. E. Moore predicted in 1969.[3]

At present, IC manufacturers are using the KrF laser at a wavelength of 248 nm to write circuits on wafers, producing CMOS chips at the 130 nm node (90 nm gate lengths). According to SEMATECH's technology roadmap for semiconductors, 197 nm lithography technology has passed through research and development and is ready to be used for semiconductor industries for mass production applications. Following 193 nm, 157 nm is the candidate for optical lithography technology to produce ICs at the 65 nm and 45 nm nodes.

Table 1.2. Roadmap of Lithography Technologies and their corresponding nodes

| Year | Node (nm) | Lithography Technology | Transistors in a single chip (million) | Processor | Wavelength (nm) |
|---|---|---|---|---|---|
| 1971 | 10000 | | 2300 | 4004 | |
| 1972 | 10000 | | 3500 | 8008 | |
| 1974 | 6000 | | 6000 | 8080 | |
| 1976 | 3000 | | 6500 | 8085 | |
| 1978 | 3000 | | 29000 | 8086 | |
| 1982 | 2000 | | 134000 | 80286 | |
| 1985 | 1500 | | 275000 | 386™ | |
| 1989 | 1000 | g line steppers | 1.18million | 486™ | 436 |
| 1993 | 800 | i line steppers | 3.1million | Pentium | 365 |
| 1997 | 350 | DUV | 7.5million | Pentium II | 248 |
| 1999 | 250 | DUV | 9.5million | Pentium III | 248 |
| 1999 | 180 | DUV | 24million | Pentium III Xeon | 248 |
| 2000 | 130 | DUV | 42million | Pentium 4 | 248 |
| 2001 | 130 | DUV | 55million | Pentium 4 with HT technology | 248 |
| 2003 | 90 | VUV | | | 193 |
| 2005 | 65 | VUV | | | 193 -> 157 |
| 2007 | 45 | VUV->EUV | | | 157 -> 13 |
| 2009 | 32 and below | EUV | | | 13 |

Source: Intel

For an optical material to be a candidate lens material for a particular lithography system, it should have high transmittance/low absorptance (the ratio of radiant flux absorbed to incident energy) and a high damage threshold at the target wavelength. Thus, ultrahomogeneous optical glasses were used with i line lithography. They were replaced by fused silica, with its higher transmittance and damage threshold compared to ultrahomogeneous optical glasses, at 248 nm and 193 nm. At 157 nm even fused silica is too absorptive, so that it does not transmit sufficient light and is easily damaged by irradiance by short wavelength UV lasers. Transmissive optics at 157 nm can be made with crystalline fluorides such as LiF, $MgF_2$, $BaF_2$ and $CaF_2$. LiF can only be used as a backup material as its mechanical softness and hygroscopic nature make polishing it difficult and it readily develops absorptive color centers. $MgF_2$ is naturally birefringent (birefringence - a property of optic material due to which its refractive index changes with polarization of light) and can't be used for optic elements. $BaF_2$ have high intrinsic birefringence making their usage in lens systems limited. $CaF_2$, because of its excellent UV transmission, high laser damage threshold and resistance to chemical effects, is considered as the primary candidate lens material at 157nm lithography.[4] It was first thought that $CaF_2$ did not exhibit intrinsic birefringence, but a recently discovered small birefringence is complicating lithographic stepper lens design.[5] According to ISMT, the effect of intrinsic birefringence in $CaF_2$ can be corrected by using a combination of lens elements made from (111) and (100) $CaF_2$ crystal materials.[6]

## 1.1. Research motivation:

In an optical lithography system, optical components should show no appreciable degradation after a large number of high fluence laser pulses. With minimum feature size reduced to the order of a nanometer, even a small degradation in the stepper tool can produce a catastrophic effect on the performance of a fabricated device and results in reduced yield (ratio of dice working satisfactorily to the total number of dice produced from a wafer).

Degradation and destruction of optical elements results mainly due to contamination of their surfaces. Contamination can occur during the manufacture of optics or during the lithography process itself. In the later case, the optical elements used in stepper tools can become contaminated in multiple ways, including outgassing of other components, gas borne volatiles or adsorption of water vapor from the ambient.

In the optics manufacturing process, the optical surfaces are polished to attain the proper optical figure and cleaned using different solvents to remove particulate and molecular contamination that absorb incident laser energy. The adverse effect of the polishing process results in surface defects such as microcracks, sleeks, scratches, pits, dislocations and disordered surface layers on the optical surfaces. These surface defects can trap and adsorb contaminants such as water and hydrocarbons from the atmosphere or from the polishing liquids themselves. Contaminants on dielectrics can increase the temperature of the surface locally to a few thousand degrees Kelvin when the dielectric is irradiated by a short pulse laser, resulting in damage of substrate.[7] Table 1.3 shows the percentage of energy loss in an optical lithography system due to a 1nm layer of water contamination on one and ten optical surfaces at different wavelengths.[8] In modern lithography tools, the number of optical elements is usually greater than five, so that ten optical surfaces is a conservative estimate.

Table 1.3. Percentage energy loss with water on optical surfaces

| Wavelength (nm) | Absorption Coefficient ($cm^{-1}$) | Energy loss with 1 surface (%) | Energy loss with 10 surfaces (%) |
|---|---|---|---|
| 248 | $4.81\times 10^{-3}$ | $4.8 \times 10^{-8}$ | $4.8 \times 10^{-7}$ |
| 193 | $1.63 \times 10^{-1}$ | $1.7 \times 10^{-6}$ | $1.6 \times 10^{-5}$ |
| 157 | $1.73 \times 10^{5}$ | 1.7 | 16 |

As seen from the above table, absorption of light energy by water contamination at 157 nm is considerable whereas it is negligible at other wavelengths. Particulate contamination can be avoided by maintaining clean fabrication rooms and molecular contamination can be removed using cleaning by solvents. The removal of molecular contamination by solvents is efficient up to the 193nm wavelength as the solvents do not absorb significant energy, but at wavelengths such as 157 nm and below these solvents strongly absorb incident laser energy.

In addition to the intrinsically absorbing contaminants, absorbing contaminants may be produced via photoreaction of initial contaminants with the light source to produce new products with enhanced the absorption of the incident light energy. This process is termed as photocontamination. For example, a monolayer (≈ 3 $A^0$) of hydrocarbon photodeposit on an otherwise transparent optical component will attenuate 1% of incident light energy at 157 nm.[9]

E. Eva et al. (248 nm), C. Gorling et al. (193 nm and 157 nm) and T. M. Bloomstein (157 nm) showed that the absorptance of transparent optical materials was reduced significantly after multiple laser pulse irradiations.[10-12] Figure 1.1 shows the reduction in absorptance of $CaF_2$ as a function of total irradiation dose at 157 nm.[11] The strong reduction in absorptance is due to photo-induced desorption of contaminants from the surface.

Surface roughness and defects on optical elements result in loss of contrast and intensity in the optical image formed due to scattering and stray light in optical systems.[7] Surface roughness is the measure of smoothness of the surface an optical element. Ideally, an optical surface should be smooth.

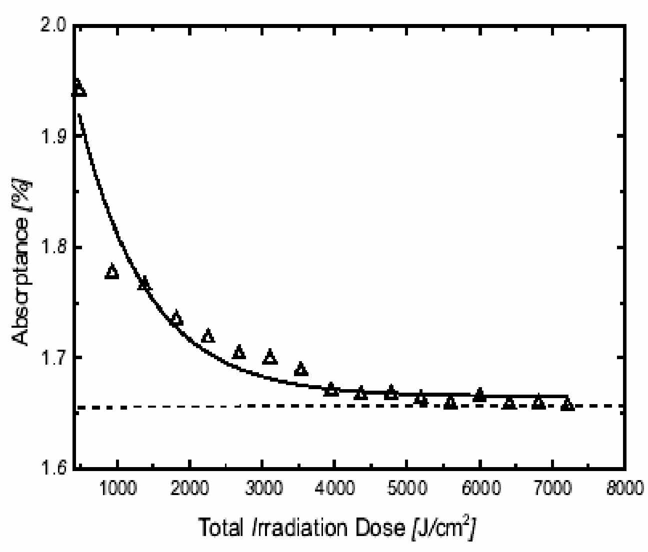

Figure 1.1. Absorptance of $CaF_2$ vs. Total Irradiation Dose, at 157nm

Therefore, mitigation of contamination of optical surfaces is necessary and LID was used to desorb contaminants from optical surfaces before they could be photopolymerized into larger, more adherent contaminants. Use of an infrared laser as a desorption source also helped prevent photopolymerization or other photolysis reactions. In order to clean optical surfaces effectively, the different types and amounts of adsorbed species on optical surfaces must be identified. This allows the optimization of parameters such as laser wavelength, energy and pulse width to produce an efficient cleaning process.

## 1.2. Overview of the study:

In this work, LID in combination with TOF-MS was used to determine the amount of water and hydrocarbons desorbed from $CaF_2$ samples, without damaging the surface of the substrate. The lenses in photolithography tools are curved and investigating surfaces that deviate from cleavage planes is essential. In this study, 10°

and 15° off-axis (100) $CaF_2$ samples along with (100) and (111) $CaF_2$ samples were analyzed and same LID experiments were carried out on all the samples. $CaF_2$ is cubic and cutting it by a certain off-axis in any direction from a cleavage plane results in same surface structure. In chapter 2, a brief review of theory of LID and TOFMS is presented. Literature related to laser cleaning and adsorbate analysis using laser desorption is also reviewed. The significance of surface topography of optical elements in an efficient lithography system is also included. In chapter 3, the experimental setup used to conduct the different experiments along with schematics and actual setup pictures is provided. The threshold model used in this work to analyze different desorbed species is also discussed. Chapter 4 discusses water and hydrocarbon desorbed species maps plotted using experimental data. AFM was used to investigate surface topography of different off-axis (100) orientation $CaF_2$ samples and the observed roughness of the various samples investigated is reported. Finally, conclusions are drawn from the work to date and the scope of future work is outlined.

# CHAPTER 2

# PREVIOUS WORK

This chapter presents adsorbate surface analysis with emphasis on the principle of LID, and relative advantages of LID over temperature programmed desorption (TPD) along with the various types of laser desorption techniques using laser. The TOF-MS technique for analyzing desorbed species is discussed and its relative advantages over other mass analysis techniques are also presented. The role of surface topography of an optical material in allowing good optical transmission is also discussed. Finally, a review of work that was done in the fields of removal of adsorbed species from surfaces, adsorbate analysis and surface topographical studies of transparent optical materials by various researchers along with a model developed to analyze the data obtained from desorption is presented.

## 2.1. Adsorbate surface analysis:

A well established procedure for analyzing surface adsorbates consists of desorption of adsorbed species and detection of the desorbed species. Adsorbed contaminants can be desorbed from a substrate by heating the substrate to high temperatures that can be achieved by either conventional heating of the substrate using TPD or a laser beam.

When the surface from which the species have to be desorbed is irradiated by a laser beam, a large temperature difference is produced between adsorbate and the bulk of the substrate. This produces a sudden expansion in volume of the adsorbate that allows the adsorbate molecules to overcome the Van der Waal's force or the chemical bond that binds them to the surface of the substrate, thus resulting in the desorption of adsorbed species from the substrate. The process in which a laser beam is used to desorb the adsorbate is called laser induced desorption. The desorbed species can be detected by using a mass spectrometer and later analyzed using different models.

The major advantage of LID is that it allows surface adsorbate analysis without modifying the substrate surface. In contrast, conventional surface analysis techniques such as scanning Auger microprobe (SAM) and secondary ion mass spectroscopy (SIMS) result in significant surface damage. Only a small area equal to the laser spot size is heated in LID, as it is the only region being irradiated. This allows adsorbate surface mapping to understand the distribution of contaminants on the surface of the substrate. With TPD the whole substrate is heated at the same time to induce desorption and thus mapping of adsorbed species is not possible. In addition to the advantage of localized desorption provided by LID, significantly higher surface temperatures can be achieved using laser heating, enhancing the probability of desorption of contaminants from protected sites such as defects, pits and pores.

### 2.1.1. Desorption techniques:

Desorption techniques that are currently being studied can be broadly classified into four types. They are:

#### 2.1.1.1. Desorption of particles from semiconductor devices and substrate materials:

A laser beam is used to heat substrate/particles or an energy transfer medium absorbed under and around the particles. In the first case, the substrate absorbs the laser energy and causes rapid expansion of surface and/or explosive evaporation of the energy transfer medium that results in particle removal. In the second case, particles absorb the laser energy and the force resulting from thermal expansion of particles detaches them from the surface. In the last case, the energy transfer medium absorbs the laser energy resulting in rapid evaporation of the medium thus desorbing the particle.

#### 2.1.1.2. Desorption of molecular contaminants from the surface of a substrate by laser heating the substrate material:

In this technique, the substrate is heated using a laser to flash desorb the contaminants. A pulsed infra-red (IR), visible (VIS) or ultraviolet (UV) beam can be used to desorb contaminants.

#### 2.1.1.3. Desorption of molecular contaminants from the surface of a substrate by laser heating the adsorbed contaminants:

In this technique, a laser beam is used to directly heat the contaminants. The parameters to be considered to induce desorption by laser heating the contaminants are discussed below:

2.1.1.3.1. Laser wavelength: In order to have high coupling of laser energy to the contaminants and effective removal of contaminants, the contaminants should have large absorption coefficient at the chosen wavelength (resonant absorption wavelength). For example, to efficiently desorb water molecules that have a strong absorption between 2.7 μm to 3.1 μm, a HF laser at 2.8 μm can be used.

**2.1.1.3.2. Laser pulse width:** A short laser pulse width (less than microsecond) is recommended to increase the temperature of the contaminants rapidly, without significantly affecting the underlying substrate temperature via thermal diffusion from the heated contaminants or surface. This avoids unnecessary modifications of the substrate. A very short laser pulse will increase the probability of substrate damage, as damage is usually a function of the peak laser intensity while the peak temperature depends on total laser energy on a time scale short relative to thermal diffusion.

**2.1.1.3.3. Laser energy density:** The laser energy should be maintained above the desorption threshold of the contaminants and below the damage threshold of the substrate. This helps in removing the contaminants without damaging the substrate.

### 2.1.4. Desorption by photochemical excitation of the substrate/ adsorbed contaminants that leads to reaction and/or heating:

A UV laser can be used to either create reactive gaseous species that diffuse to the surface and chemically react with contaminants or used to heat the contaminants that then react with specific reactive gases to produce desorption.

In this research work, laser induced thermal heating of the contaminants (using the resonant absorption principle) is used to desorb the contaminants from calcium fluoride. The laser wavelength is chosen such that the substrate is highly transparent but that the presumed adsorbed contaminants (in this case water) are highly absorptive. This laser/substrate/adsorbate configuration minimizes energy input into the substrate and, therefore, minimizes substrate damage.

### 2.1.2. Time-of-Flight Mass Spectrometer (TOF-MS):

The TOF-MS consists of a source-extraction region, a drift region and a detector.[13] Figure 2.1 shows the structure of a simple TOF. The source-extraction region is formed by the source back plate and extraction grid. In this region, ions are desorbed from a sample of interest (example: $CaF_2$). Typically, a potential (V) that is of same polarity as the ions to be collected is applied to the source back plate while the extraction grid is held at ground potential, in order to accelerate the ions to a constant energy (eV). Thus, the final kinetic energy of the accelerated ions is shown in equation 2.1, where 'm' is ion mass, 'v' is ion velocity and 'e' is electron charge.

$$(mv^2)/2 = eV \qquad 2.1.$$

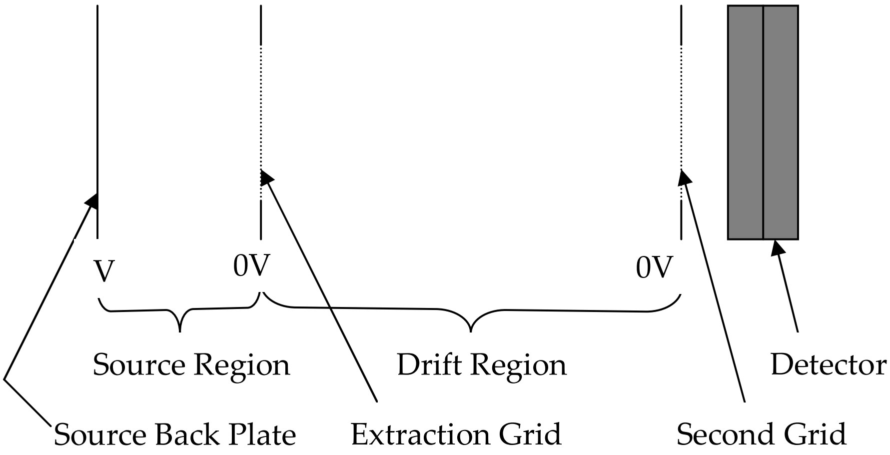

Figure 2.1. Time of Flight Mass Spectrometer

The extraction grid, along with a second grid placed in front of the detector, constitutes the drift region. Both the grids are maintained at ground potential, making the drift region field free. The accelerated ions travel through the drift region with velocities corresponding to their mass given by equation 2.2. Thus, a lighter ion travels with a higher velocity than a heavier ion and reaches the detector before the heavier ion.

$$v = (2eV/m)^{1/2} \qquad 2.2.$$

If 'L' represents the length of the drift region and 't' represents the flight or time taken by the ions to reach detector, then the flight time of ions can be represented by equation 2.3.

$$t = (m/2eV)^{1/2} * L \qquad 2.3.$$

The TOF can also operate with 0V applied to the source back plate. In this case a potential of opposite polarity to that of the ions to be collected is applied to both the grids.

As the ions always obey equation 2.3, whether or not any resolution enhancement tools are used, a TOF can be calibrated by using equation 2.4 where 'a' represents a constant of proportionality and 'b' represents a factor that accounts for any time offsets such as triggering of recording devices, laser firing time etc.

$$t = a\, m^{1/2} + b \qquad 2.4.$$

Multiple extraction regions and also energy-focusing devices such as reflectron or electrostatic energy analyzers can be incorporated in TOF to obtain better mass resolution.

The major advantage of TOF is that it can detect all the ions of different mass values that are extracted at the same time whereas the other types of mass analyzing techniques such as quadrupole mass analyzer (QMA) and double focusing magnetic sector mass spectrometers can detect, respectively, only one and a maximum of up to four mass values, at a time.[14] Other advantages of TOF include its simplicity, relatively low cost and compactness.[13]

## 2.2. Surface topography:

Understanding the surface topography of an optical material is very important in order to gain complete knowledge of its optical performance. The factors that have strong influence on the optical performance of a material are surface structure (depends on the nature of the crystal substrate), surface defects (depends on the mechanism used to grow and finish the substrate material) and surface quality (depends on the polishing, cleaning and coating techniques used to generate the finished optic). For example, optical materials that are polished using different techniques have different surface finish, resulting in different surface smoothness (measured in terms of surface roughness). Surface roughness affects the amount of light scattered out of the optical train and thus the amount of light transmitted by them differs.[15] Moreover, surface polishing processes usually result in surface defects that act as capillary spaces for adsorption and trapping of contaminants. Therefore, differently polished surfaces have different amounts and distribution of contaminants.[16] Thus surface characterization of optical materials is essential.

Surface characterization of optical components can be performed by conducting scattering measurements such as total light scattering measurements (TS) and X-ray scattering (XRS), etc., or by using different microscopy instruments such as scanning electron microscope (SEM), scanning tunneling microscope (STM), and AFM, etc. Using AFM is advantageous for investigating surface topography of insulators, as the substrate surface need not be coated with a conducting material (SEM requires a conductive surface and STM requires either a conductive or semi-conductive surface) and thus it provides a relatively nondestructive means for surface topographic analysis. Other advantages of using AFM are that it provides the highest resolution and acquires three-dimensional data in a digital format that can be used further to quantify surface structure.

Surface roughness is the major parameter that determines the amount of light transmitted and/or scattered by an optical component. Thus, optical surfaces are characterized by using various mathematical tools that calculate surface roughness. Different mathematical tools calculate surface roughness differently, so an accurate tool that describes a particular surface should be selected to obtain good analysis of the surface.[15] Typically, Root Mean Square (RMS) roughness, Power Spectral Density (PSD) and autocovarience are used to measure roughness of a surface using AFM and are described briefly below:[16 - 18]

2.2.1. **RMS roughness** is the simplest among the three tools and calculates standard deviation of height and thus describes the distribution of heights about the mean value. It is used to analyze surfaces that have Gaussian or near-Gaussian height distributions, i.e., surfaces with more degree of spatial randomness.

2.2.2. **PSD** is the Fourier decomposition of an image into spatial frequencies and thus uses a spectrum of wavelengths to approximate the surface. It is used to characterize surfaces that have periodic variations in height.

2.2.3. **Autocovarience** is the inverse Fourier transform of the product of the Fourier transform and the complex conjugate. It uses spatial correlation of heights and is used to measure some set of correlation lengths in an image such as atomic spacing.

An AFM can be used in contact mode or tapping mode or non-contact mode to obtain a topographic image of a surface. Every mode has its advantages and disadvantages.[19] In contact mode, the probe tip of AFM is dragged across the surface of the sample. A constant force is maintained between the tip and the sample irrespective of the surface height variations and the distance the tip moves in order to keep the force constant gives the topography of the surface. The major advantage of this mode is that it is capable of measuring atomic resolution images on clean surfaces. In tapping mode, the tip lightly taps on the sample surface contacting the surface at the bottom of its swing. In this mode, the tip always tries to maintain a constant oscillation amplitude of the tip and any changes due to surface variations are stored as a topographic image. The major advantage of this mode is that it uses lower forces and thus soft samples can be imaged with less damage. In the last mode of interest i.e., non-contact mode, the tip never touches the surface of the sample but oscillates above an adsorbed fluid layer on the sample surface to obtain the topographic image. In non-contact mode, either a constant amplitude or frequency of tip oscillations is maintained. The main disadvantage of this mode is lower lateral resolution (limited by the tip-sample separation) compared to both contact and tapping modes.

In this work, AFM was used to characterize the surface of $CaF_2$ samples in contact and tapping modes and RMS surface roughness was calculated.

## 2.3. Review of previous work:

Significant work has been done in the area of laser desorption of contaminants using different desorption. L. P. Levine et al. reported that water vapor, CO and $CO_2$ were desorbed from Ni and Si films using LID in 1967 using QMA to detect the desorbed neutral species.[20] S. M. Bedair removed atomic contaminants such as carbon, oxygen etc., from nickel using a Q-switched ruby laser in 1969.[21]

Cleaning of optical components has been explored relatively recently.[22, 23] T. J. Chuang used a $CO_2$ TEA laser for excitation of $SF_6$ to etch silicon.[23] He also used a quadrupole mass spectrometer to observe desorbed species. He reported that the effect of photo-radiation at the gas-solid interface on the surface reaction was significant and that LID of $SF_6$ was a necessary step to etch silicon.

W. Zapka et al., N. S. McIntyre et al., A. Bodemann et al., K. Yamaguchi et al., S. Boughaba et al., J. C. Lu et al. and S. D. Allen et al. are a few among numerous groups that demonstrated laser removal of particles on various sample materials satisfactorily.[24-30]

Cleaning of highly transparent optical materials has been studied by comparatively less number of groups.[10, 11, 31-33] S. D. Allen et al.[31] used a pulsed infrared laser source (HF/DF) to desorb water and hydrocarbons from optical surfaces such as $CaF_2$, NaCl etc. The adsorbates were desorbed in Ultra-High Vacuum (UHV) conditions and the desorbed species were detected using a quadrupole mass analyzer. Their study was mainly concentrated on water because different studies reported it as common contaminant of optical surfaces and coatings.[33-38] They first demonstrated laser desorption analysis as a viable nondestructive technique for characterization of optical surfaces in 1982.[31, 39]

The H. K. Park group constructed and implemented a practical laser based tool using a KrF excimer laser that can successfully remove sub micron-sized particulates and organic films.[40] The tool provides a cleaning rate of over 200 cm/min. Their cleaning tool utilizes a laser assisted particle removal theory that is similar to the one developed by the S. D. Allen group.[41]

### 2.3.1. Adsorbate surface analysis:

Experiments performed by the S. D. Allen group showed that normal heating of optical materials such as $CaF_2$, $BaF_2$ and NaCl to 250° C at $10^{-8}$ T – $10^{-9}$ T for 8 -12 hours did not remove water and hydrocarbons.[39] This was confirmed later when LID removed water from the same substrates. In the same work, they also reported that LID cleaned areas dosed with many Langmuirs of $H_2O$ (both at room temperature and –100° C) did not retain water at room temperature, as no desorbed fluence was detected when the same areas were reirradiated later. They also observed large site-to-site variation of desorbed fluence from the same sample and under the same experimental conditions.[31,39] The theory developed from these results was that the adsorbed species are generally located in surface defects such as scratches, pits, microcleavages, dislocations and disordered surface layers.

Because of the fast heating rates afforded by a nsec pulsed laser, LID using such a system probably involved explosive evaporation or boiling. Such a process normally has a very high activation energy and can, therefore, be characterized as exhibiting a threshold-like desorption behavior. In other words, there is a minimum laser energy density (threshold density) necessary to start desorption of an adsorbed species. It is assumed that above a threshold laser energy density all the adsorbed molecules are desorbed. The fact that, desorption involving a laser is a highly nonlinear process justifies the threshold concept. S. D. Allen et al. used a simple mathematical model as described below to determine the threshold laser energy density of water in their study.[39, 42]

The Gaussian laser beam used to induce desorption is represented by equation 2.5 where '$\phi$ ' is the instantaneous energy density, '$\phi_o$' is the axial energy density, 'r' is the radius of the Gaussian beam at $\phi$ and '$\rho_o$' is the radius of the Gaussian beam when intensity falls by $\phi_o/e$ value of the axial value.

$$\phi (r) = \phi_o \exp (- r^2/\rho_o^2) \qquad 2.5.$$

For normal incidence on a flat substrate, laser intensity equal to or greater than threshold intensity ($\phi_{th}$) on a particular site irradiates a circular area corresponding to $r_{th}$ as given by equation 2.6.

$$\phi_{th} = \phi_o \exp (- r_{th}^2/\rho_o^2) \qquad 2.6.$$

The area covered by a Gaussian beam increases as the axial laser energy density is increased, thereby increasing the area from which contaminants are desorbed (only when $r \geq r_{th}$, i.e., $\phi \geq \phi_{th}$). As depicted in Figure 2.2 with laser energy densities $\phi_1 > \phi_2 > \phi_{th}$ (since, $I_2 > I_1 > I_{th}$), the radii of cleaned area corresponding the two beams holds the relation $r_{th2} > r_{th1} > r_{th}$. Therefore, desorption fluence ($\Psi$) is directly proportional to the irradiated area and can be represented by equation 2.7, where m is a constant of proportionality.

$$\Psi = m \pi r_{th}^2 \qquad 2.7.$$

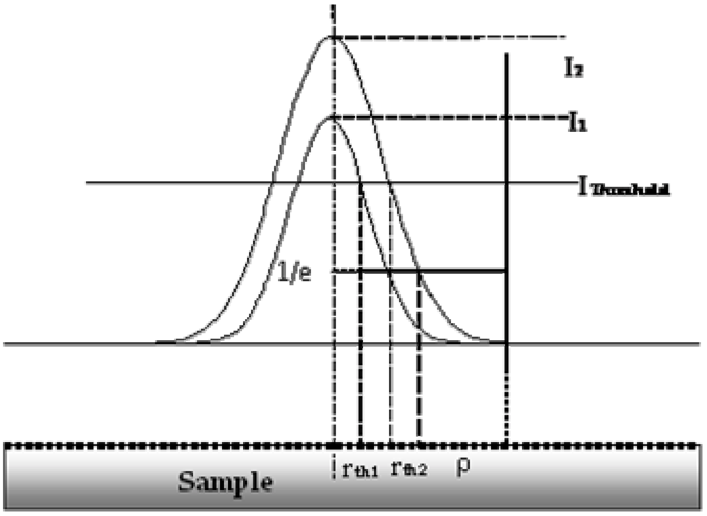

Figure 2. 2. Schematic representation of Gaussian beam at two intensities

From equations 2.6 and 2.7, the threshold energy density can be related to desorption fluence as given in equation 2.8.

$$\Psi = m \pi \rho_o^2 [ \ln (\phi_o) - \ln (\phi_{th}) ] \qquad 2.8.$$

A plot of $\Psi$ vs. $\phi_o$ gives a straight line with the slope proportional to the beam area and average contaminant surface concentration and intercept equal to the threshold energy density of the LID process for a particular contaminant molecule.

The S. D. Allen group also observed that, with an HF laser used to irradiate $CaF_2$, the laser damage threshold for $N(\phi_0)/1$ technique (multiple laser shots on one site) was higher than the 1/1 technique (one laser shot on each site). In the $N(\phi_0)/1$ technique, each site on the surface is first irradiated by a low laser energy density laser beam where no desorption can be obtained and then the laser energy is increased gradually, keeping the same spot size. At each laser energy, N nominally identical pulses are used to irradiate the surface. In other work, J. O. Porteus et al. showed that the damage threshold of a NaF film nearly doubled after exposure to multiple nondamaging pulses.[43] They stated that spatially selective laser damage on a substrate is due to "impurity aggregation".[44] The increase in laser damage threshold with LID is attributed to a laser preconditioning or cleaning effect. To be more specific, a site first irradiated by a laser beam of relatively low energy density desorbs some water and other contaminants and possibly anneals some surface defects. Further cleaning and/or annealing takes place when the same site is irradiated by a slightly higher laser energy density, resulting in an overall increased surface laser damage threshold.

The S. D. Allen group also reported high desorption efficiency for water with HF laser (2.8 μm) compared to DF laser (3.7 μm).[31] This is because water has a strong absorption at 2.8 μm. S. M. Durbin et al. used a frequency tripled/quadrupled Nd:YAG laser to clean oil and grease from steel in 1998.[45] They effectively removed oil-based contaminants from microcavities using 266 nm laser beam, which is strongly absorbed by hydrocarbon films and the underlying steel substrate, with an approximate energy density of 100 mJ/cm$^2$ Another laser beam at 355 nm wavelength (not strongly absorbed by the hydrocarbon contaminant films) with an energy density greater than 25 J/cm$^2$ damaged the substrate significantly before significant contamination removal was accomplished. From these experimental results, it is evident that using a laser wavelength that is strongly absorbed by adsorbed contaminants results in higher cleaning efficiency.

O. Kreitschitz et al. used TOF-MS to conduct LID of $SrF_2$, $CaF_2$ and $MgO_2$ to investigate the dependence of yield and kinetic energies of positive ions at 193 nm and 308nm wavelengths.[46] They mainly observed metal ions such as $Sr^+$, $Ca^+$, $Mg^+$ and molecular ions such as $SrF^+$, $CaF^+$ and $MgO^+$. In their subsequent work, they have investigated the relationship between emission yield and laser energy per pulse (E) and reported that emission yields increase on the order of $E^n$ where n was related to defect-initiated neutral particle emission and gas-phase ionization.[47] M. Reichling et al. also explored LID of positive ions desorbed from $CaF_2$ substrates at 532 nm to understand the relationship between optical transmission and laser energy density.[48] In their following work, they used photoacoustic mirage technique to determine the ablation threshold of different optical materials such as $CaF_2$, $BaF_2$, $MgF_2$ and LiF with different polishing techniques.[49] In all the above examples, the laser energy densities were much higher than those used in the present work, resulting in ablation of the substrate itself. As previously discussed, the substrate surface damage threshold is a strong function of the surface preparation technique, with samples that are rough or that contain significant amounts of entrained polishing solvents or other contaminants damage at a significantly lower value than “clean” surfaces.

## 2.3.2. Surface topography:

S. R. Rebecca et al. investigated $CaF_2$ with two surface qualities resulting from mechanical polishing (MP) and chemical-mechanical polishing (CMP).[16] They used optical interferometry and AFM to correlate transmittance and surface roughness. They tested transmittance from 185 nm to 400 nm. They reported that transmittance at 193 nm, increased from 90.3 % with MP to 91.98 % with CMP. Surface roughness calculated for MP was 1.4 nm and for CMP was 0.8 nm. They stated that the decrease in roughness and increase in transmittance was due to elimination of mid- and high-spatial frequency roughness (caused by subsurface damage that accompanies MP) in CMP.

D. Angela et al. investigated the surface finish of standard polished and superpolished $CaF_2$ samples.[17] They developed totally automated instruments to measure total backward and forward scattering of optical components down to 157 nm. The group used total light scattering measurements (TM), X-Ray Spectrometer (XRS) and AFM in their work and used PSD to calculate surface roughness by AFM. They reported that low and mid spatial frequencies had different roughness levels. They also plotted two-dimensional scattering maps for the two surface qualities using TS measurement and reported that superpolished samples had a very low scatter level that can be compared to high quality fused silica.

R. Bennewitz et al. performed scanning force microscopy of as-cleaved and electron irradiated $CaF_2$ samples, using contact and noncontact modes, in UHV.[50] They reported that freshly cleaved surfaces can be imaged in contact mode with high resolution and electron-irradiated surfaces in non-contact mode due to strong adhesive forces between tip and metal enriched surfaces with contact mode scanning.

## 2.4. Summary:

An N/1 LID process with a laser wavelength that is highly absorbed by contaminants can be used to obtain efficient removal of contaminants without damaging the substrate. The different contaminants desorption thresholds can be determined using the model established. Furthermore, using a combination of LID and TOF-MS, molecular contaminants desorbed from a substrate can be analyzed and surface maps of different contaminants can be obtained. This technique allows the measurement of the different contaminants, their densities and their distribution on a substrate. With such information, modifications can be made to conventional processing to optimize the polishing and cleaning process. On the other hand, AFM can be used as non-destructive surface characterization tool to gain knowledge of surface roughness of optical elements.

# CHAPTER 3

# EXPERIMENTAL

This chapter presents the experimental setup used for LID of $CaF_2$ and analysis of desorbed species after LID. Sample handling and sample loading procedure (into UHV chamber) are also presented. The desorption threshold model developed to analyze adsorbates on $CaF_2$ is also presented.

## 3.1. LID TOF-MS experimental setup:

The overall experimental setup is divided into three parts, namely LID setup, TOF setup and UHV system. Figure 3.1 shows the schematic of the experimental setup consisting of the LID setup and the TOF setup along with the UHV chamber. The small circles on the UHV chamber represent various ports of the chamber.

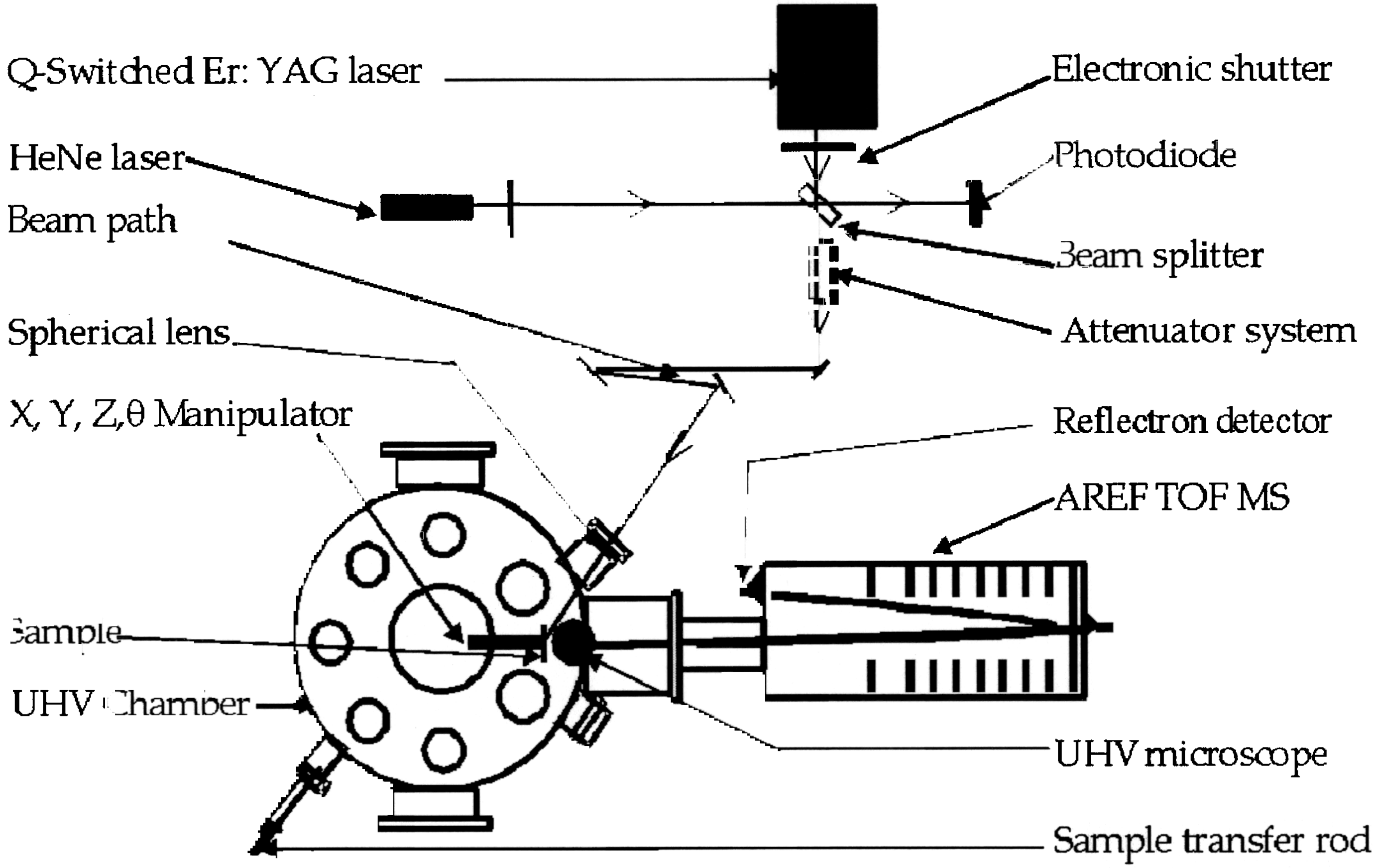

Figure 3.1. Schematic of experimental setup
Optical train, UHV chamber and TOF are shown in the diagram.

### 3.1.1. LID setup:

An Er:YAG laser (LaserSight Technologies Inc., formerly Schwartz Electro-Optics Inc., Orlando, FL) was used as the light source for LID. 2.94 µm is strongly absorbed by water molecules, a presumptive contaminant of optic materials, and not absorbed by the $CaF_2$ substrate. The Q-switched laser operates at a wavelength of 2.94 µm and a pulse length of 100 ns FWHM. The advantage of using larger pulse length compared to pulsed solid state lasers such as Nd:YAG is increased damage threshold. Damage threshold increases linearly with the square root of the pulse length.[51] As the natural pulse length of the Er:YAG is 250 µs, a Q-switch controller (Lincoln laser company, Phoenix, Arizona) was used with the laser to obtain a shorter pulse. 250 µs is too long to effect the explosive evaporation necessary for LID. The rotating mirror Q-switch motor speed was set at 200 RPS and its lever wheel switches were set at 63 to obtain a pulse repetition rate of 2 Hz. The laser was operated in $TEM_{00}$ mode with the help of an intra-cavity aperture. The laser beam profile was Gaussian. A pyroelectric detector (Pyrocam II, Spiricon) was used to confirm the beam profile. Figure 3.2 shows a picture of the actual LID setup used in the current work. A HeNe (633 nm) laser beam was aligned collinear to the Er:YAG laser beam in order to trace the path of the laser beam and also to locate the laser spot on the sample surface. A UHV compatible microscope attached to one of the reentrant optic port of UHV chamber was also used, in addition to HeNe laser, to find the laser beam on the sample. An electronic shutter was placed at the output of the Er:YAG laser to control the time duration between pulses, producing single shot irradiation conditions in order to avoid any residual effects of a previous pulse. The maximum output energy of the laser was 20 ± 1 mJ/pulse. A photo detector (Molectron detector, Pyroelectronic joulemeter, Model J25) was used to measure the beam energy. A small fraction of the laser beam was diverted to another photo detector (Molectron detector, model P5-01) using an AR-coated beam splitter and was used to ensure that a constant delay (i.e., ionization period - explained in section 3.2.2) was maintained between the laser signal and pulser pulse. The beam splitter has transmission greater than 95 % at 2.94 µm and reflectance greater than 80 % at 633 nm. The laser beam passed through an optical system consisting of an attenuator system and a beam steering system. The attenuator system is comprised of glass slides with a thickness of 1mm. Each glass slide transmits 78 % to 80 % of the incident energy at 2.94 µm. An appropriate number of filters were used to obtain different energy levels required for investigating desorption thresholds of the different contaminants on $CaF_2$. The beam steering system consists of four gold-plated copper mirrors. The mirrors were aligned such that the laser beam enters the UHV chamber and hits the sample through a reentry window tube of the UHV chamber that contains a spherical focusing lens (f = 150 mm). The angle of incidence of laser beam on the sample is $60^o$, producing an elliptical spot size with major and minor axes ($D_{1/e}$) of 720 µm and 360 µm respectively.

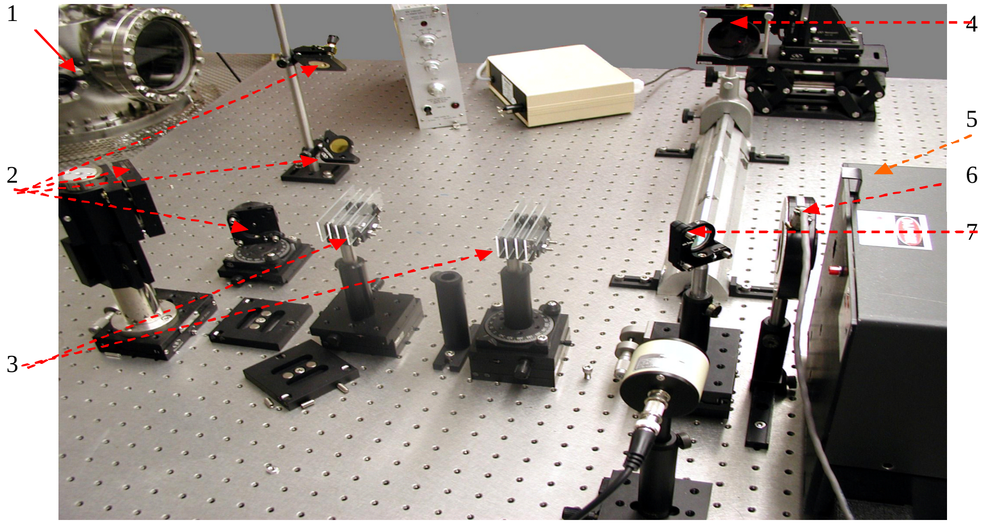

Figure 3.2. Actual LID setup

1. Spherical lens 2. Beam steering mirrors 3. Variable attenuation system
4. HeNe laser 5. Er:YAG laser 6. Electronic shutter 7. Beam splitter

## 3.1.2. TOFMS setup:

The TOFMS assembly (R.M. Jordan) consists of a repeller plate ($A_1$), an extraction grid ($A_2$), an acceleration plate ($A_3$), a linear detector, an angular reflectron detector and an electron gun system as shown schematically in Figure 3.3. Figure 3.4 shows the photo of the TOF plates that were used in the current work. The sample was placed close to the repeller plate as shown in Figure 3.4. The small separation (˜ 1 mm) between the sample and the plate $A_1$ allows the sample to be scanned relative to the fixed laser beam.

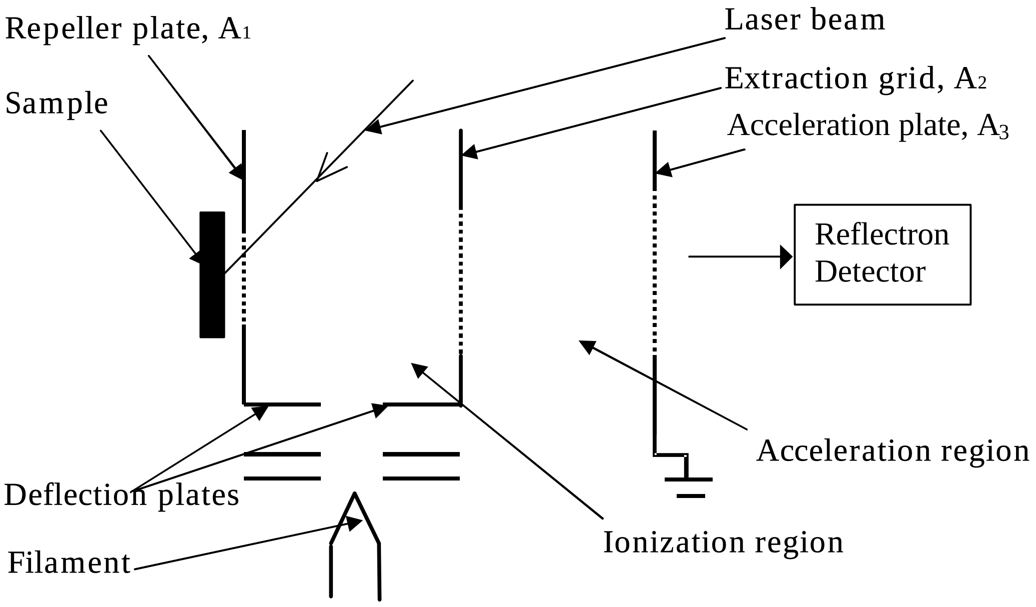

Figure 3.3. Ionization region

Electron impact ionization was used to ionize the desorbed species. A tungsten filament located in the center of the space between the repeller plate and the extraction grid as shown in Figure 3.4 produced the electron beam required for ionization. The advantage of electron impact ionization (EI) is that almost all molecules can be ionized by EI and EI fragmentation mechanisms are well understood. Several sets of deflection plates were used to control the electron beam alignment.

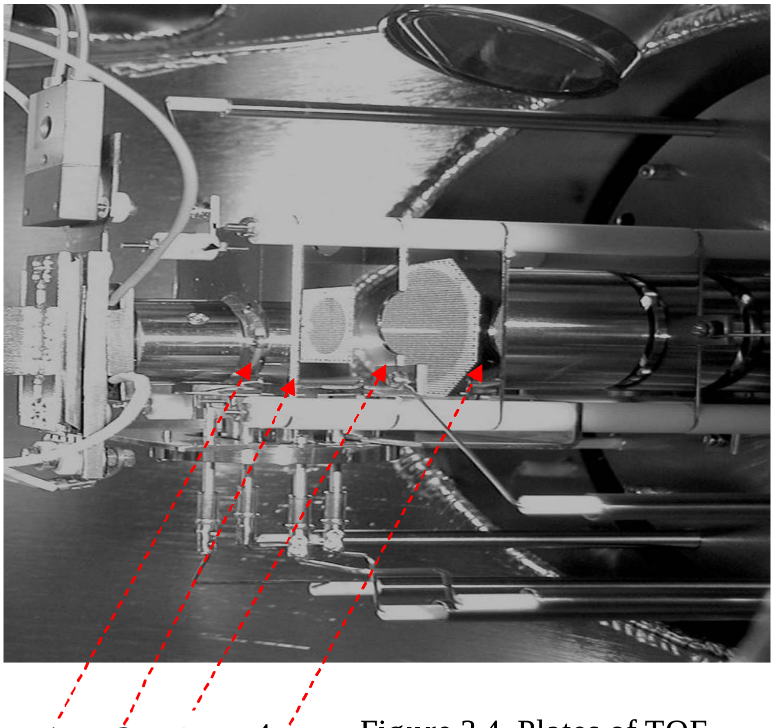

Figure 3.4. Plates of TOF

1. Sample
2. Repeller plate
3. Extraction grid
4. Acceleration plate

A voltage $V_{A1}$ equal to 1200 V was applied to the plate $A_1$. The plate $A_2$ was connected to a high voltage remote pulser power supply and a voltage $V_{A2}$ equal to 800V was applied, which was less than the repeller plate voltage ($V_{A1}$). Before and after the laser fires, $V_{A1} > V_{A2}$, and the electron beam bends towards the repeller plate and out of the ionization region between $A_1$ and $A_2$. A remote pulser that produces a pulse of 400 V with a rise and fall time of 10 ns was added to the voltage on plate $A_2$; a certain time after the laser was fired. The timing of the laser pulse and pulser pulse along with the changing plate voltages is shown in Figure 3.5. When the potential on $A_1$ and $A_2$ were equalized, the electron beam enters the region between the two plates and ionizes the species that were desorbed by laser beam. The time period during which the potential on both plates remains equal is called the ionization period. After time $T_3$, the potential on the plate $A_2$ returns to 800 V and remains there until the next pulse is given.

Any ions that were created during the EI pulse are extracted into the acceleration region between plates $A_2$ and $A_3$. The time delay between the laser shot and the leading edge of the pulser pulse was adjusted to correspond to the arrival of the LID molecular pulse in the ionization region. Matching the EI pulse with the LID pulse optimizes the signal to noise as background gas ions are created in the ionization region only during the short time the LID pulse is there. Optimum values for the delay time ($T_1$ – $T_2$), the ionization period ($T_2$ – $T_3$), electron energy and electron current were set at 0.1 µs, 7 µs, 60 eV and 0.5 mA, respectively.

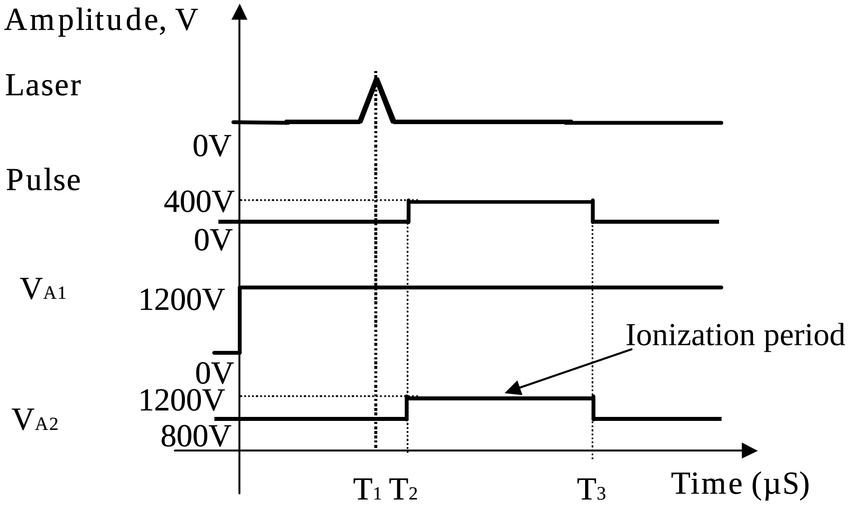

Figure 3.5. Schematic of timing sequence of different voltages.
Period between $T_2$ and $T_3$ is the ionization period

The TOF-MS consists of two detectors, a linear detector and a reflectron detector. The linear detector was used while calibrating the TOF. The angular reflectron detector (AREF) eliminates random background ions and was used during the reported experiments. The AREF detector was maintained at –4000 V. The reflectron operation was obtained by maintaining the retarding grid and the reflector grid at 700 V and 1150 V respectively. The data from the TOF was displayed on a digital oscilloscope (Lecroy Wavepro 940) with 10 ns resolution and stored on a Pentium IV system for analysis. Microsoft Excel and Origin were used to analyze and plot the data.

### 3.1.3. UHV system:

A UHV environment is required to conduct the adsorbate analysis experiments in order to maintain a contamination free environment during the experiment. Figure 3.6 shows the schematic of the UHV system (Perkin - Elmer, model TNB-X) used in the current work. The UHV chamber was supported by an ion pump with pumping speed of 220 L/S, a turbo pump with 60 L/S backed by a rotary vane pump with 1.5 $m^3$/hour, a titanium sublimation pump, nitrogen source and a controller unit. The turbo pump, nitrogen source and sample transfer rod were connected to the UHV chamber near the sample chamber, through a butterfly valve and a gate valve as shown in Figure 3.6.

Figure 3.7 shows a picture of the turbo pump and the ion pump. The pressure in the UHV chamber was read using either an ion gauge or thermistor gauge depending on the pressure range. The thermistor gauge (used to measure pressure in both sample and UHV chambers) reads from $9.9 \times 10^{-2}$ T to $1 \times 10^{-3}$ T and the ion gauge (used to measure pressure in the UHV chamber) reads from $5 \times 10^{-3}$ T to $2 \times 10^{-11}$ T.

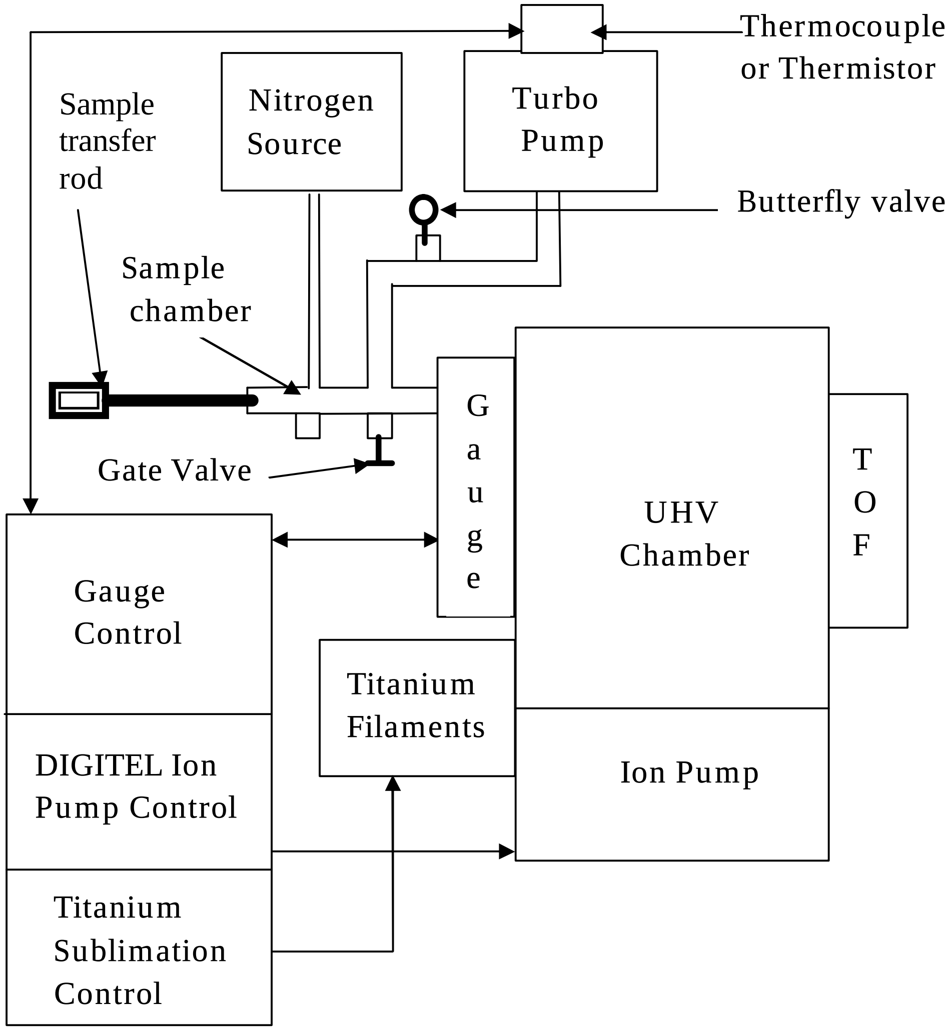

Figure 3.6. Schematic of UHV system

The controller unit consists of various switches to operate different gauges and titanium sublimation pump control switches as shown in Figure 3.8. In the gauges section, the controller has an autocross that automatically switches from the thermistor gauge to the ion gauge and vice versa according to the pressure inside the chamber. An X, Y, Z and θ sample manipulator (Vacuum Generators, model HPT-RX) was attached on the top of the UHV chamber as shown in Figure 3.9. The sample was placed inside the sample loadlock chamber and a sample transfer rod is used to load/unload the sample. The sample transfer rod consists of three prongs that correspond to three holes on sample holder, as shown in Figure 3.10.

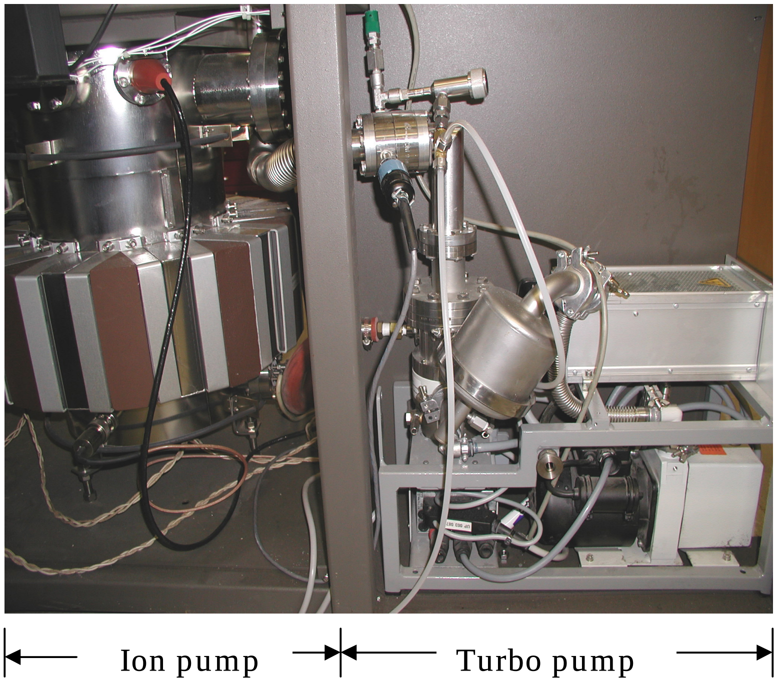

Figure 3.7. Actual Ion pump and turbo pump

Turbo pump was used to initially pump down the pressure to $1 \times 10^{-5}$ T and then the ion pump was used to pump down to the order of $10^{-9}$ T. The system was then baked out at $120^{\circ}$ C for 30 hours. The pressure in the UHV chamber was $1 \times 10^{-10}$ T after bake out and maintained at $3 \times 10^{-10}$ T after repeated loading and unloading of samples. A quadrupole mass analyzer (Stanford Research Systems, model RGA-100) attached to a port of the UHV chamber was used to analyze the background gas.

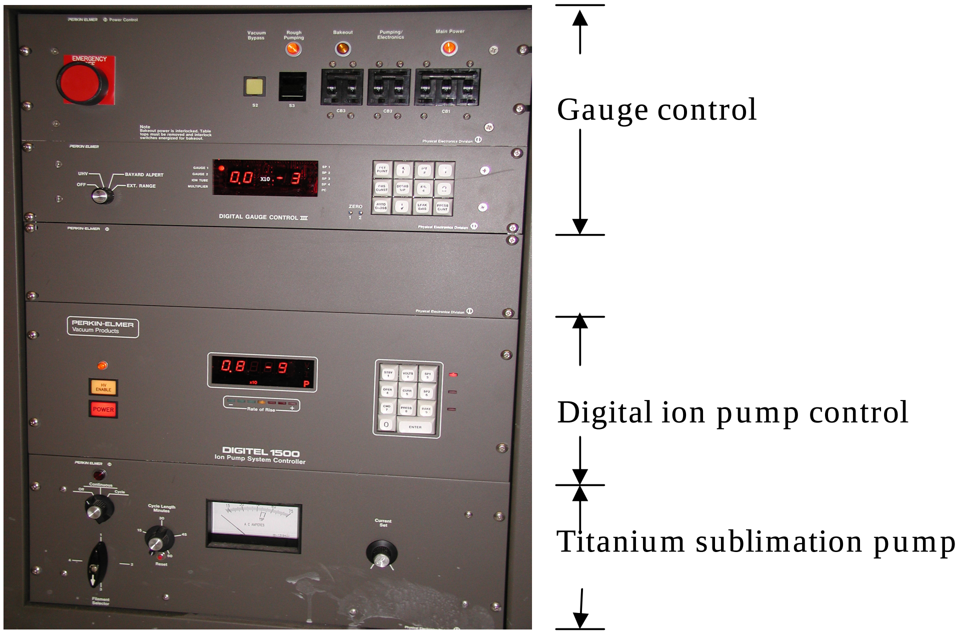

Figure 3.8. UHV system controller

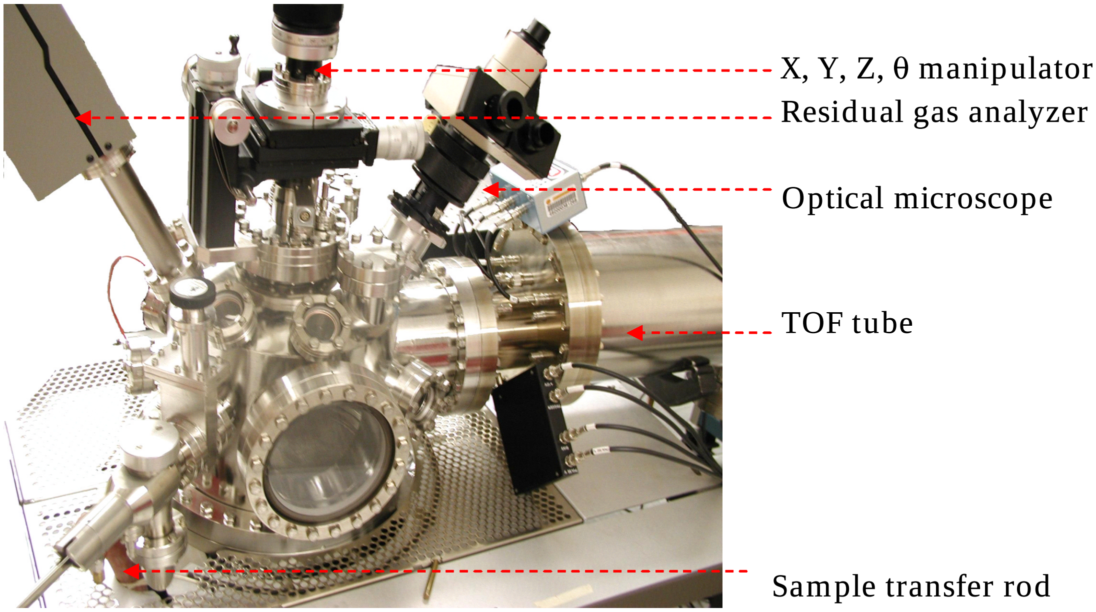

Figure 3.9. UHV Chamber with X, Y, Z, θ sample Manipulator

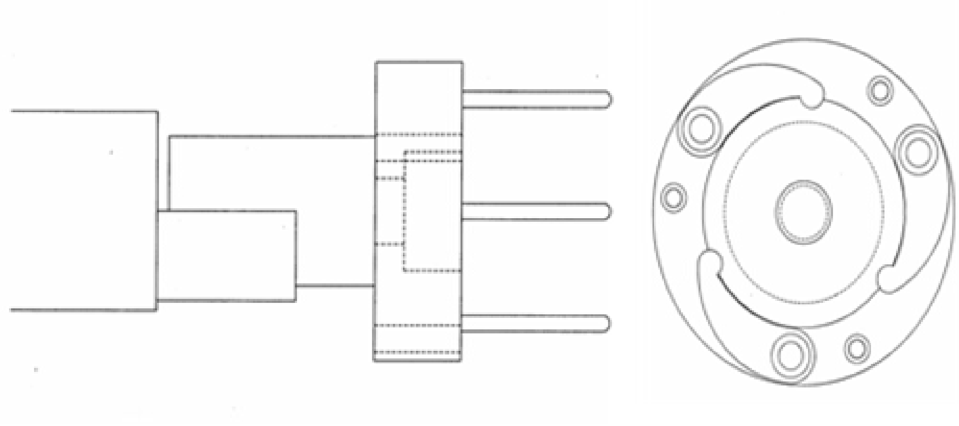

Figure 3.10. Sample transfer rod and Sample holder

## 3. 2. Sample handling:

The different off-axis cut $CaF_2$ (100) samples were obtained from St. Gobain/Bicron. All the samples were mechanically polished by the manufacturer. Removal of polishing residue on the surface of the samples was done by first rinsing with soapy water and then wiping with a dry tissue. Later the samples were cleaned with tissue moistened with methanol and acetone (1:1). The 12 mm diameter samples were used, as they were received from the manufacturer. Prior to loading into the UHV chamber the samples are stored in vacuum desiccator to avoid surface adsorption from the ambient.

The samples were observed initially under an optical microscope with 10X magnification and no particles were seen on the surface except for occasional scratches.

## 3. 3. Sample holder and its preparation:

The sample holder has a circular opening to hold the sample. The sample was fastened to the holder using three clips and three screws that were $120^{o}$ apart as shown in Figure 3.10.

First the sample holder was rinsed with isopropanol and then it was cleaned ultrasonically for 15 minutes in 2-propanol. After cleaning, the clips and the screws were oven dried. During drying they were covered with aluminum foil to keep off dust. A Pyrex glass plate of 1 cm thickness was placed inside the sample holder (behind the sample) to absorb the transmitted laser energy and prevent stray reflected beams. The sample holder has a large diameter, coarse-threaded screw mount for attachment to the sample mount on the manipulator. The combined sample holder and sample mount is placed close to the source back plate of the TOF. A 1200 V potential is applied to the sample mount to nullify the electric field effects from the high voltages in the ion source region.

## 3. 4. Sample changing:

Initially, the ion pump was turned off in order to bring up the pressure inside the UHV chamber. The X, Y, Z, θ scales of the sample manipulator were adjusted to bring the sample in alignment with the sample transfer rod height and position. After the pressure reaches $1 \times 10^{-6}$ T, the butterfly valve was closed to block the air in the tube connecting the turbo pump to the UHV chamber from entering the chamber. At this point, the ion gauge was also turned off to avoid its damage due to an increase in pressure inside the UHV chamber when the sample transfer rod is pushed in. The gate valve was then opened to allow the passage of the sample transfer rod to the sample manipulator. Using the sample transfer rod, the sample holder was unscrewed from the sample holder manipulator and brought back to the differentially pumped sample chamber. Now, the gate valve was closed and nitrogen gas was pumped into the sample chamber to bring up the pressure in the sample chamber to atmospheric pressure. When the thermistor gauge reads beyond scale, the sample chamber cap was opened and the sample was changed using tongs.

A new sample mounted on the sample holder is placed on the sample transfer rod and the lid covering the sample chamber was tightened. After closing the sample chamber, the nitrogen gas purge was stopped and the butterfly valve was opened to pump down the sample chamber. After the thermistor gauge reads $10^{-3}$ T, the pressure was pumped down further for 15 to 30 minutes to ensure that the actual pressure inside the sample chamber was below the pressure that can be read by the ion gauge. Autocross on controller was turned on and the gate valve was opened slowly. The sample holder was screwed to the manipulator using the sample transfer rod after the ion gauge read $9 * 10^{-7}$ T. The ion gauge was again turned off to pull back the sample transfer rod to its extreme position. The butterfly valve was again opened to pump down the pressure in the UHV chamber to less than $10^{-6}$ T. The gate valve was closed when the ion gauge read $1 * 10^{-6}$ T. The ion pump was opened to pump down the pressure to the order of $10^{-9}$ T for 24 hours. At this stage, the sublimation pump was used along with ion pump to pump down the pressure to the order of $10^{-10}$ T.

## 3. 5. AFM experimental setup:

In this work a scanning probe microscope (Digital Instruments model DI 3000) was used in contact and tapping modes to measure the surface nanotopography of the $CaF_2$ sample surfaces. In the contact mode, a silicon nitride probe (Model DNP) with a tip radius of curvature of 5 to 10 nm and spring constant of 0.58 N/m were used. In the tapping mode, silicon probes with a tip radius of curvature of 30 nm and spring constant of 30 - 60 N/m were used.

The lateral resolution of an AFM is limited by two factors, tip radius and pixelization (smallest resolvable feature change), whichever is larger. The vertical resolution is limited by three factors, vertical scanner movement (<1 $A^o$), pixelization (smallest resolvable height change determined by the conversion of 16bits over the full vertical range of the scanner) and overall system noise (0.3 to ˜1 $A^o$ RMS), whichever is larger.

For all the scans taken, samples per line parameter was set at 512 x 512 pixels in X and Y scan directions to obtain the maximum lateral resolution available. The probe tip was installed on the AFM cantilever holder and was loaded at the bottom of the piezo. The AFM laser was aligned on the tip and the photodetector was adjusted to measure the reflection of light from the tip. The microscope was aligned to the tip to visually observe the area to be scanned. The sample to be scanned was then placed below the AFM probe and the sample surface was brought into focus to select an area to scan. For contact mode all the initial scan parameters such as scan size (1 µm), scan rate (1 Hz), scan angle ($0^o$), X and Y offsets (both 0), integral gain (2.0) and proportional gain (3.0) etc., were set and the tip was engaged with the surface of the sample. In the tapping mode, cantilever tuning was initially done to obtain the resonant frequency of tip oscillations and then the parameters (same as in contact mode except for integral gain (0.5) and proportional gain (0.7)) were set and the tip was engaged on the surface. Once a good tip engagement was ensured, scan parameters were adjusted to obtain desired scan size and scan rate, etc. After the image was captured, flattening (third order) of the image was performed to remove the Z offset between scan lines and the tilt and bow in each scan line. Later, the images were analyzed using the different tools available (such as section and roughness) to investigate the topography of the scanned surface.

## 3. 6. Degenerate threshold model:

In this work, the defect density and contaminant adsorption on a surface are assumed to be uniformly distributed over the small analysis area for the purposes of analyzing defect mediated adsorption. Such defect densities and contaminant concentrations are expected to vary significantly from analysis site to analysis site. It is also assumed that adsorption occurs preferentially at surface defects and there is a minimum laser energy density called the threshold energy density necessary for desorption to take place. Thus, above the threshold density all the adsorbate molecules are assumed to be desorbed. A mathematical model as described below was developed to quantitatively analyze the experimental data in this current work.

In the current work, the incident angle (θ) of laser beam on the sample was 60° to the normal to the surface whereas it was 0° in previous work. This provides improved cleaning efficiency.[52] Since the beam is not normal, the spatial distribution of a Gaussian laser beam is elliptical. Figure 3.11 gives the cross sectional view of a Gaussian beam where $r_a$ and $r_b$ represent the radii along major and minor axes. Equation 3.1 gives the representation of a Gaussian beam when incident angle is other than zero, x and y represent the radii of the area cleaned by the laser beam along major and minor axes directions respectively.

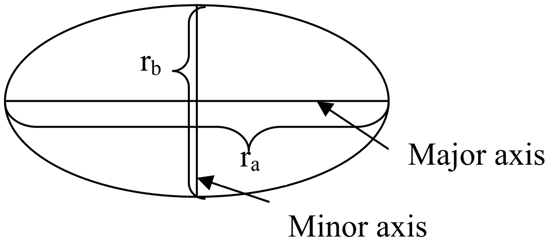

Figure 3.11. Cross sectional view of a Gaussian beam when incident angle ≠ 0°

$$\phi = \phi_o \exp - [(x/r_a)^2 + (y/r_b)^2] \qquad 3.1.$$

A 2-D representation of the elliptical Gaussian beam, shown in Figure 3.12, gives equation 3.2 ($\rho_o$ represents 1/e radius of the Gaussian beam). In this figure $r_b$ is perpendicular to the plane of the paper. The radius of the elliptical laser beam perpendicular to the plane of the paper, i.e., along the minor axis of the ellipse, is given by equation 3.3.

$$r_a = \rho_o / \cos\theta \qquad 3.2.$$

$$r_b = \rho_o \qquad 3.3.$$

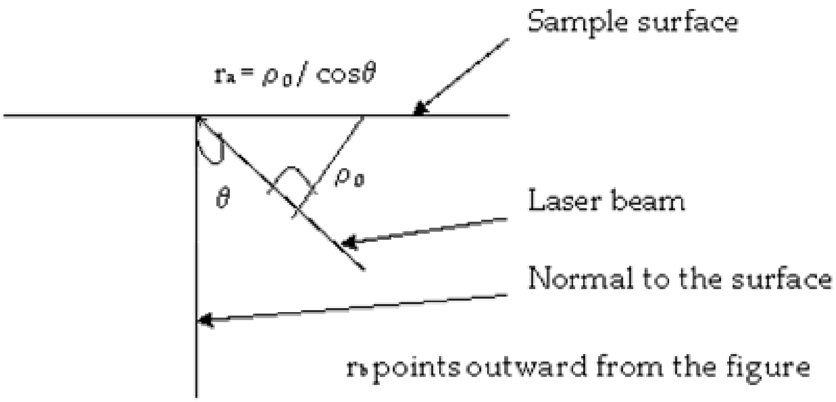

Figure 3.12. Schematic representation of the mathematical model

When $\phi = \phi_{th}$, the radii of the area cleaned along the major and minor axes of the laser beam are given by $x = r_{a\,(th)}$ and $y = r_{b\,(th)}$. At the threshold energy density equation 3.4 modifies to equation 3.5.

$$r_a = r_b / \cos\theta \tag{3.4.}$$

$$r_{a\,(th)} = r_{b\,(th)} / \cos\theta \tag{3.5.}$$

Solving equation 3.1 for the desorption threshold energy density (i.e., $\phi = \phi_{th}$) gives equations 3.6 and 3.7.

$$\phi_{th} = \phi_o \exp - [(r_{a\,(th)} / r_a)^2] \tag{3.6.}$$

$$\phi_{th} = \phi_o \exp - [(r_{b\,(th)} / r_b)^2] \tag{3.7.}$$

Equating equations 3.6 and 3.7 gives the relationship between actual radii and the radii of the cleaned area (threshold radii) as in equation 3.8.

$$r_{a\,(th)} / r_a = r_{b\,(th)} / r_b \tag{3.8.}$$

Solving equations 3.6 and 3.7 for the threshold radii along major and minor axes of the beam gives equation 3.9 and 3.10 respectively.

$$r_{a\,(th)} = r_a^2 \, ( \ln \phi_o - \ln \phi_{th} ) \tag{3.9.}$$

$$r_{b\,(th)} = r_b^2 \, ( \ln \phi_o - \ln \phi_{th} ) \tag{3.10.}$$

Substituting equations 3.3 and 3.4 in equation 3.9 gives equation 3.11. Similarly substituting equation 3.3 in 3.10 gives 3.12.

$$r_{a\,(th)} = (\rho_o^2 / \cos\theta \,) \, ( \ln \phi_o - \ln \phi_{th} ) \tag{3.11.}$$

$$r_{b\,(th)} = \rho_o^2 \, ( \ln \phi_o - \ln \phi_{th} ) \tag{3.12.}$$

As desorption fluence ($\Psi$) is directly proportional to the irradiated area above the threshold laser energy density (refer section 2.3), desorption fluence can be obtained from equation 3.13.

$$\Psi = m\, \pi\, r_{a\,(th)}\, r_{b\,(th)} \qquad 3.13.$$

Substituting $r_{a(th)}$ and $r_{b(th)}$ from equations 3.11 and 3.12 in equation 3.13 results in desorption fluence given by equation 3.14.

$$\Psi = m\, \pi\, (\rho_o{}^2 / \cos\theta)\, [\, \ln \phi_o - \ln \phi_{th}\, ] \qquad 3.14.$$

Therefore, desorption threshold energy density is given by the intercept of a plot of ln $\phi_o$ vs. total desorption fluence at a particular site.

In the experiments, laser energy (E) was measured and axial laser energy density was calculated as explained below. Equation 3.1 was integrated from -∞ to +∞ with respect to both x and y as in equation 3.15.

$$E = {}_{-\infty}\!\int^{+\infty}{}_{-\infty}\!\int^{+\infty} \{\phi_o \exp - [(x/r_a)^2 + (y/r_b)^2]\}\, dx\, dy \qquad 3.15.$$

The integral was solved using error function and the resulting equation is given in equation 3.16.

$$E = \phi_o\;\; \pi\, r_a\, r_b \qquad 3.16.$$

Substituting the $r_a$ and $r_b$ values from equations 3.2 and 3.3 in 3.16, gives equation 3.17.

$$E = \phi_o\;\; \pi\, \rho_o{}^2 / \cos\theta \qquad 3.17.$$

$$\therefore \qquad \phi_o = E \cos\theta \,/\, (\pi\, \rho_o{}^2) \qquad 3.18.$$

Thus, the relationship between axial laser energy density and laser energy is given by equation 3.18.

# CHAPTER 4

# RESULTS AND DISCUSSIONS

This chapter presents the results of LID-TOFMS measurement of thresholds and mapping of contaminants on several on and off-axis (100) $CaF_2$ samples. The mass peaks detected on $CaF_2$ samples and their attribution to different ions are discussed. The determined desorption threshold energy density values for water and hydrocarbons at particular sites and the reason for existence of multiple thresholds at some sites are also discussed. Numerous plots comparing the threshold energy density and desorption fluence at various sites on a sample that help in discussing the results obtained are included. The desorption fluence of water and hydrocarbons from different samples are compared. 2-D and 3-D surface maps of water and hydrocarbons on (100), $10^o$ off-axis (100) and $15^o$ off-axis (100) $CaF_2$ samples are provided. Finally AFM scans of the three types of samples along with roughness are also presented.

## 4. 1. Detected Mass Spectra:

The typical ions detected by the TOF AREF detector when (100) $CaF_2$ samples were irradiated by an Er:YAG laser beam included water ions, hydrocarbon ions, oxygen containing hydrocarbon ions and alkali metal ions. The different adsorbates and their concentration on a sample surface are distinguished by their mass to charge ratio (m/z) value and ion intensity value of the LID signal respectively. A peak with m/z = 18 is attributed to water ($H_2O$). Peaks with m/z values from 12 to 15 and from 24 to 29 are attributed to one carbon and two carbon hydrocarbon ions respectively ($C_xH_y^+$) while peaks with m/z = 23 and 39 are attributed to sodium ($Na^+$) and potassium ($K^+$) respectively. The source of hydrocarbons and oxygen containing hydrocarbons is assumed to be alcohol, a compound used in cleaning samples after the polishing process. The occasionally observed $Na^+$ and $K^+$ ions are assumed to derive from physical contact of sample with human skin during handling. Peaks with m/z values with 16 and 17 are also attributed to water ions ($OH_x^+$) as the standard electron impact ionization of alcohol doesn't show peaks at these mass values.

When background gases in the UHV chamber were examined using an RGA, only $H_2$, $H_2O$, $N_2$ and $CO_2$ were detected. When the sample is irradiated by the laser, with electron beam switched off, no ions were detected by the AREF TOF. This implies that the electron beam only ionizes the desorbed species. Figure 4.1 shows the desorption signal from two different sites on the $CaF_2$ (100) surface when irradiated by 2.94 μm wavelength light. The laser energy density used at these sites was 2.5 J/cm$^2$. The desorption spectra from the first site as shown in Figure 4.1.1 is simple and has a dominant peak corresponding to water with m/z = 18 and ion intensity ≈ 22. It also has hydrocarbon ions ($C_xH_y^+$) and oxygen containing hydrocarbon ions ($C_2H_4O^+$) at m/z = 42, 43 and 44 with much less ion intensity ≈ 2. At a different site, site 2 in Figure 4.1, the mass spectra is entirely different. The desorbed species consists mainly of hydrocarbon ions ($C_xH_y^+$, $x = 1$ to $7$ and $y = 2x + 1$) and oxygen containing hydrocarbon ions (such as $CH_2O^+$ and $C_2H_4O^+$ with m/z = 30 and 44). As intact molecular ions were not detected, it is difficult to specify the exact hydrocarbon composition. The spectra also has Na+, K+ and water ions with m/z = 23, 39 and 16 to

18 respectively. At this site, the ion intensity of the water (m/z = 18) desorption signal (≈ 12) is much less than to the highest signal ion intensity (≈ 31) detected for hydrocarbon ions (at m/z = 28). On this and other $CaF_2$ samples, the type of contaminant and their concentration varied from site to site with more complex spectra at sites with heavier contamination.

In the current work, only water ions (m/z = 16, 17 and 18) and hydrocarbon ions (m/z = 12, 13, 14, 15, 24, 25, 26, 27, 28 and 29) were quantitatively analyzed. An N/1 technique (N shots of the same laser energy density on one site) was used to clean multiple sites and two considerable facts were observed. The first was that the first laser shot always produced the maximum number of desorbed species (mass values) with the highest ion intensities (peak values), and that ion intensity of the desorbed species decreased rapidly on subsequent laser pulses. The second observation was that no molecular LID fluence was detected after consecutive multiple irradiations of the same energy density, at almost all the sites for all the samples. A plot depicting these observations is given in Figure 4.2. The laser energy density used at this site was 4.43 $J/cm^2$). With the first laser pulse H, $H_2O$, Na, $CH_2$, $CH_3$, $CH_4$ and $CH_5$ were detected with peak values of 7, 17, 8.5, 12, 7.5, 8.5 and 14.5, respectively, while with the second laser pulse $H_2O$, $CH_4$ and $CH_5$ with peak values 12, 11 and 2 were detected. As can be seen from the figure no desorption signal was detected after the first few consecutive laser irradiations. We can conclude that the surface was being cleaned and also that little or no surface readsorption occurred between consecutive laser irradiations.

At some sites, occasionally m/z = 59 ($CaF^+$) and 137 ($CaF_2CaF^+$) were observed. It is believed that these signals were not due to the ablation of the bulk surface, but were from the already damaged surface layer produced during polishing, which remained on the surface after cleaning. [53]

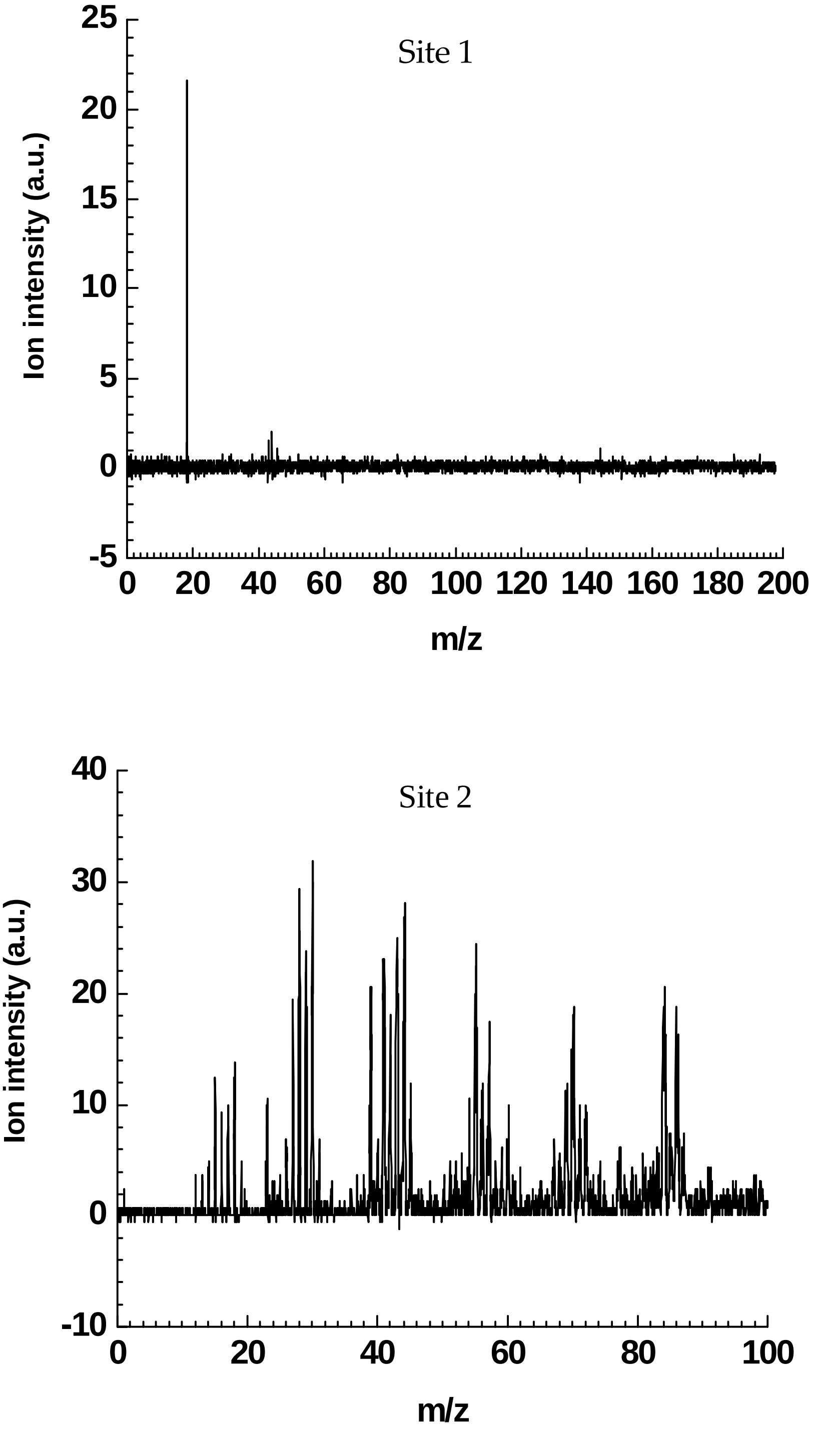

Figure 4.1. Mass spectra of desorbed species from $CaF_2$ (100) at two different sites hit with same energy Er:YAG beam

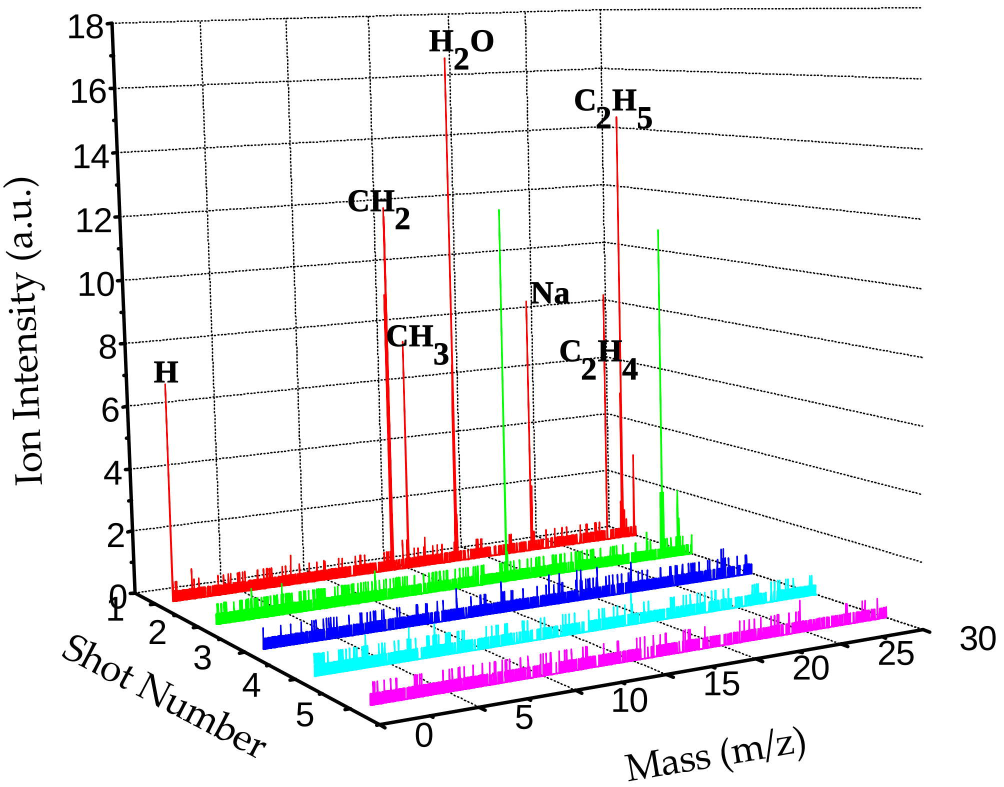

Figure 4.2. Mass spectra of desorbed species from $0^0$ off plane cut $CaF_2$ (100) surface for five consecutive laser shots of same energy density (4.43 J/cm$^2$)

## 4.2. LID threshold energy density calculation:

The N($\phi_0$)/1 technique (refer 2.3.1) was used to determine the threshold energy densities at various sites on the surface of the samples. At each laser energy five nominally identical pulses were used to irradiate the sample. In the current work, the maximum laser energy density used in all the experiments was < 7 J/cm$^2$ (equivalent to 70 MW/cm$^2$). For multiple irradiations on one site, the maximum laser damage threshold energy density of $CaF_2$ was reported to be ≈ 10 GW/cm$^2$.[61] Thus with the laser energy density used in the current work, no damage should occur on the $CaF_2$ surfaces.

In the degenerate threshold model described in section 3.6, cumulative desorption fluence (the sum of the desorption fluences from the lowest energy density used to the particular laser energy density) was used instead of desorption fluence at a particular laser energy density. Because of large site-to-site variations in adsorbed contaminants, 1/1 experiments could not be used. In this and previous work, it appears that areas of fractions of $mm^2$ are sufficiently uniform to result in consistent LID thresholds. The values measured are, of course, an average over the area irradiated, but they do provide unique LID thresholds.[31] Cumulative desorption fluence and axial energy density were plotted as shown in Figure 4.3, to determine desorption threshold energy densities of water and hydrocarbon species. The minimum laser energy density used at this site was 0.49 $J/cm^2$. Hence, to get the cumulative desorption fluence at $\phi_0 = 3\ J/cm^2$, the desorption fluences at the water (m/z =16, 17, and 18) and hydrocarbon (m/z = 12, 13, 14, 15, 24, 26, 27, 28, and 29) peaks from 0.49 $J/cm^2$ to 3 $J/cm^2$ were summed (8 shots in this case). As seen from the plot below, the LID threshold energy density ($\phi_{th}$) of water and hydrocarbons given by the x-intercept, are ≈ 1 $J/cm^2$ and ≈ 1.6 $J/cm^2$ respectively.

LID threshold energy density plots at some sites resulted in two distinct straight lines as shown in Figure 4.4. The difference in slopes implies the presence of two distinct types of defects at a site. The initial desorption was from a defect with a relatively low LID threshold energy density. At higher laser energy densities, desorption occurred from a second defect with a higher LID threshold energy density. The relatively low LID threshold energy density and the high LID threshold energy density are termed as first desorption threshold energy density ($\phi_{th1}$) and second desorption threshold energy density ($\phi_{th2}$).

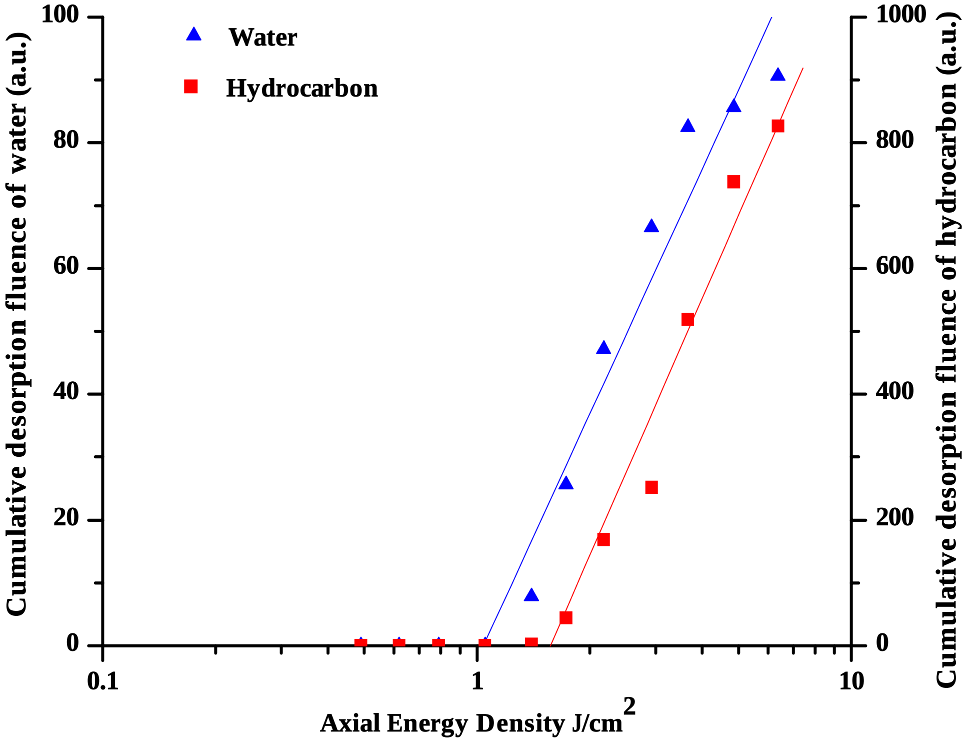

Figure 4.3. Threshold energy density plot of water and hydrocarbon desorbed fluence on $CaF_2$ (100) surface

The site in Figure 4.4 has $\phi_{th1}$ = 0.5 J/cm$^2$ and 0.45 J/cm$^2$ and $\phi_{th2}$ = 3 J/cm$^2$ and 1.8 J/cm$^2$ for water and hydrocarbon respectively. The threshold energy density of hydrocarbon ions is less than that of water which may be due to laser induced thermal desorption of adsorbate.[54] Although the hydrocarbon molecules do not strongly absorb 2.94 µm, desorption could be achieved by thermal heating of water molecules surrounding the hydrocarbon molecules. As the boiling point of hydrocarbons is less than that of water, hydrocarbons are desorbed before water. At the site shown in Figure 4.4 the hydrocarbon desorption threshold energy density is higher than that of water ions, which could be due to hydrocarbons being produced from oxygen containing hydrocarbon ions. In this case, the O-H bond absorbs 2.94µm as efficiently as water.

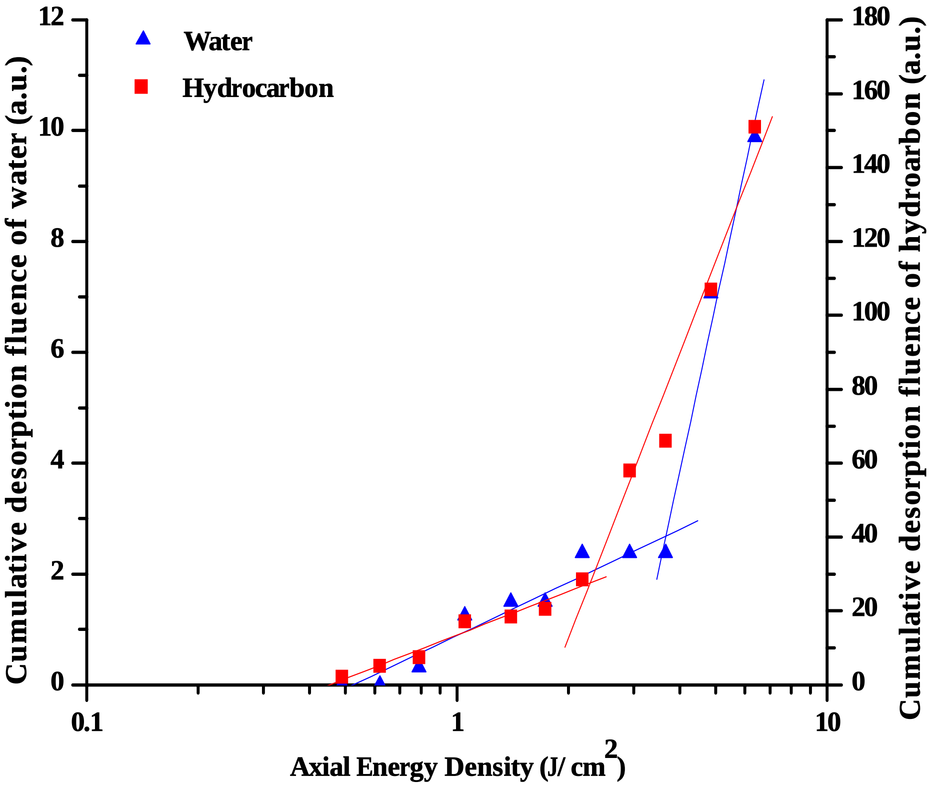

Figure 4.4. Threshold energy density plot of water and hydrocarbon desorbed fluence on $CaF_2$ (100) surface at a site with two defects

At some sites considerable desorption fluence was detected even with the lowest energy density used. A significant desorption fluence with the first laser irradiation could be due to a very low LID threshold defect at a particular site. If a site produces uncommonly high LID fluence with the first laser shot then that site is assumed to have foreign particles or other large defects. Such defect sites, if encountered, were not included in the quantitative analysis of the experimental data. The threshold energy density plot in that case consists of lines parallel to the x-axis, as large desorption fluence results on the first shot and no desorption fluence for subsequent shots below the normally measured LID threshold.

Many sites including the two sites shown in Figure 4.3 and Figure 4.4 have desorption fluences of hydrocarbons significantly higher than that of water. This is because the electron impact ionization efficiency of hydrocarbon ions is greater than that of water, not necessarily that the concentration of hydrocarbons was higher.

## 4.3. Threshold energy density and desorption fluence at various sites:

Variation of the threshold energy density and desorption fluence of water and hydrocarbons on (100) $CaF_2$ is given in Figure 4.5. Similar plots for $10^o$ and $15^o$ off-axis (100) $CaF_2$ samples are given in Figure 4.6 and Figure 4.7. In the (100) $CaF_2$ plot, site number 8 yields considerable desorption fluence even at the lowest energy density used in the experiment with no desorption for subsequent energy densities. This site was, therefore, assumed to have the first desorption threshold energy density less than the lowest energy density used in the experiment. In Figure 4.5, the lowest energy density (1.06 $J/cm^2$ in this case) is used in place of the first threshold energy density. On the $15^o$ sample at site number 4, no water was detected and the plot of variation of total desorption water fluence in Figure 4.7 has a break.

For all the three types of samples, as can be seen from the following figures, a site with the lowest threshold energy density does not necessarily have the highest desorption fluence and a site with the highest threshold energy density does not necessarily have the lowest desorption fluence. For example, in Figure 4.5, the highest water desorption fluence occurred at 1.65 $J/cm^2$ while the lowest threshold energy density occurred at 1 $J/cm^2$. This suggests that the total amount of desorption fluence at a site depends on local adsorbate concentration instead of the LID threshold energy density.

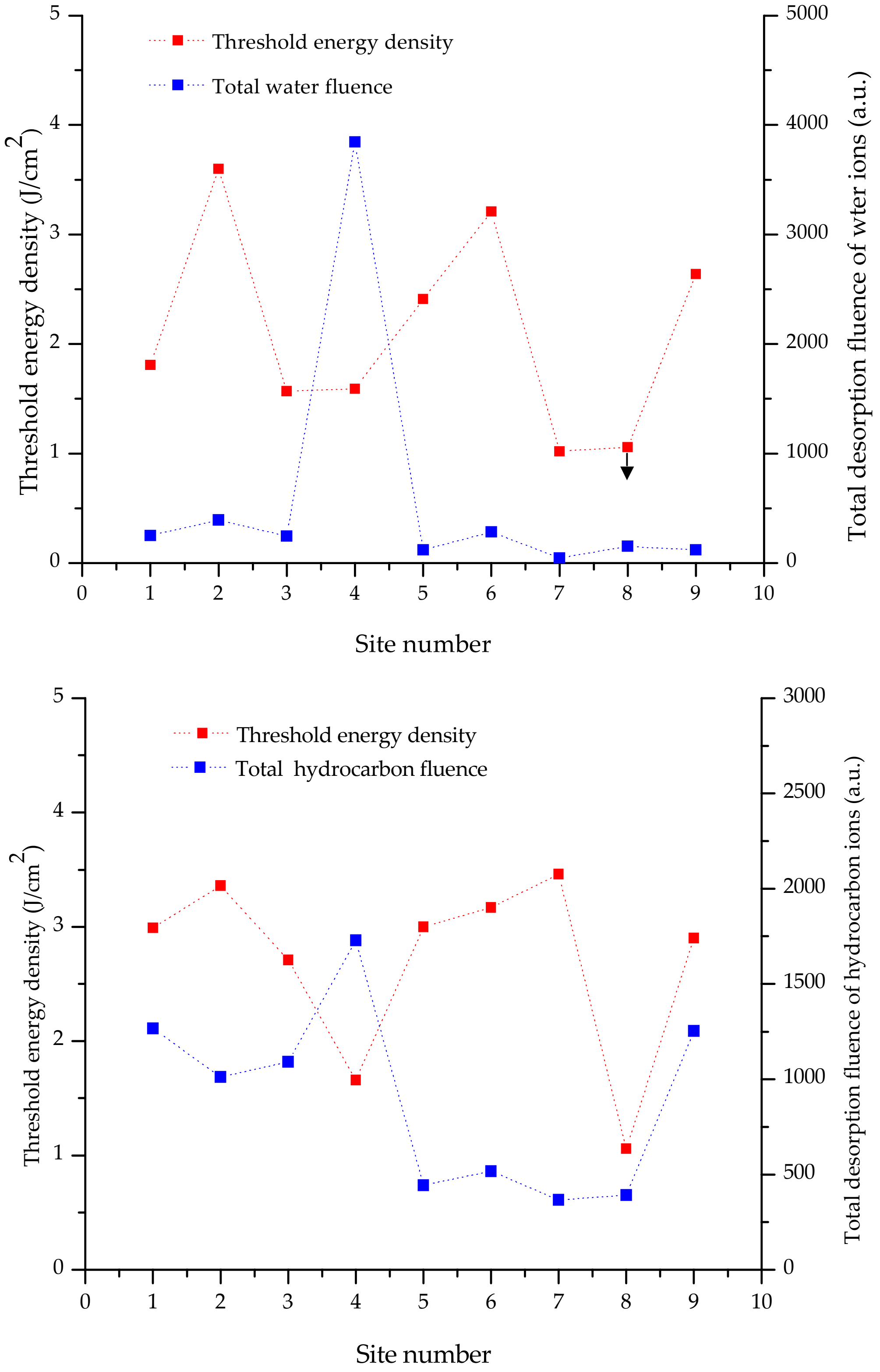

Figure 4.5. Threshold energy density and desorption fluence of water and hydrocarbons at various sites on (100) CaF$_2$ surface

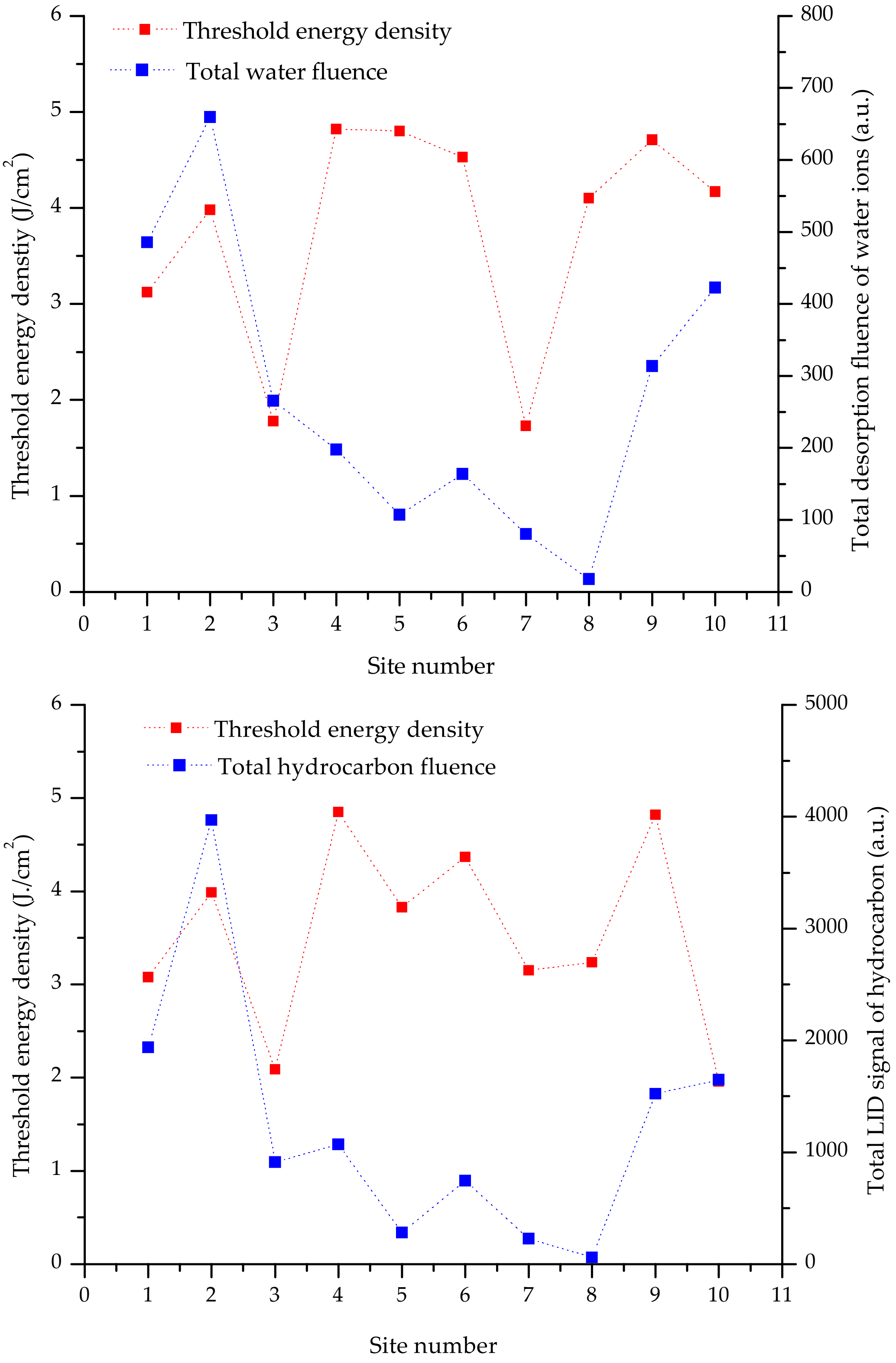

Figure 4.6. Threshold energy density and desorption fluence of water and hydrocarbons at various sites on 10° off-axis (100) $CaF_2$ surface

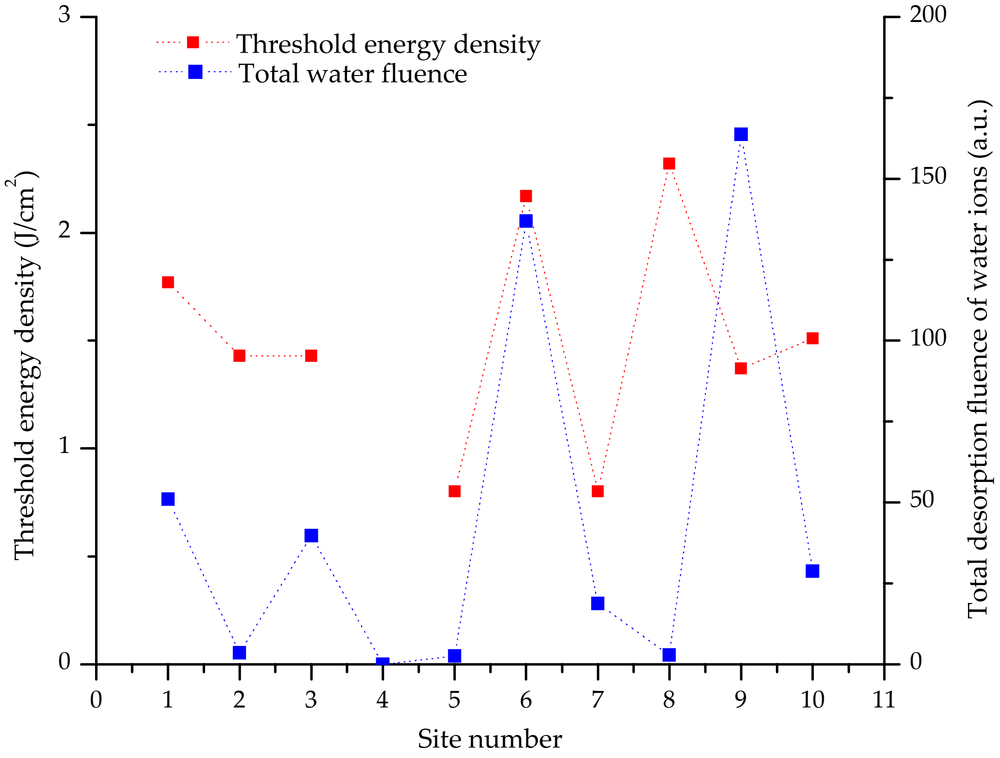

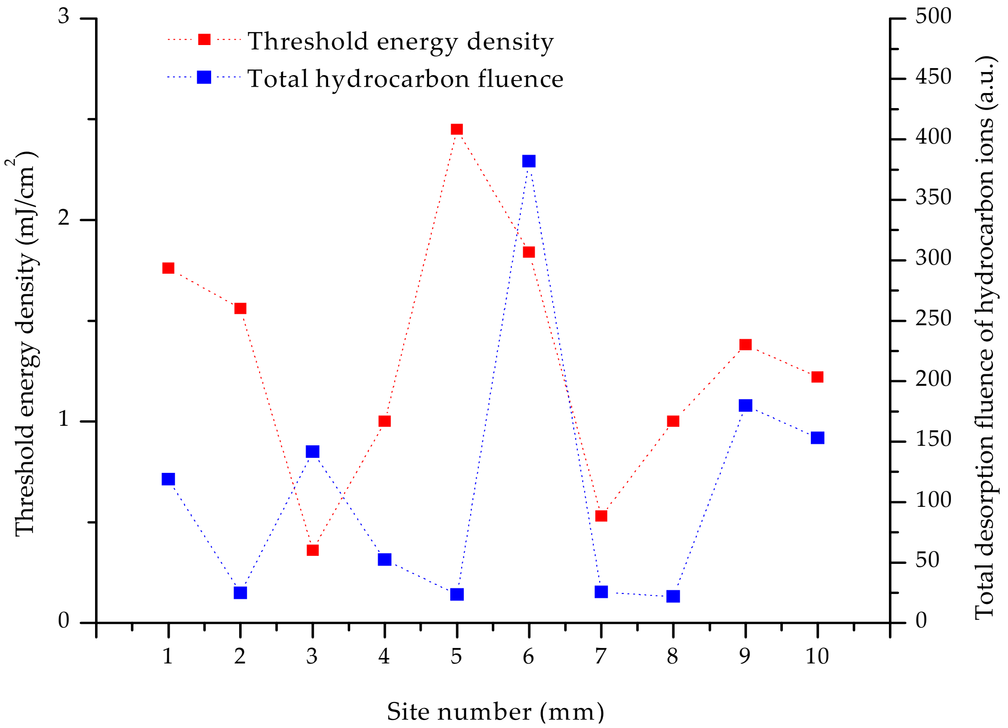

Figure 4.7. Threshold energy density and desorption fluence of water and hydrocarbons at various sites on 15° off-axis (100) $CaF_2$ surface

## 4.4. LID Threshold of different samples:

The LID thresholds determined for water and hydrocarbons on (100), $10^o$ and $15^o$ off-axis (100) $CaF_2$ surfaces varied as shown in Figure 4.8 and Figure 4.9. The plots show range (represented by bars) and the average value (represented by arrow) of LID thresholds of water and hydrocarbons LID thresholds for each sample. As seen from the figures below, the $10^o$ off-axis sample has the highest average water and hydrocarbon LID threshold value. Also, the maximum variation of water and hydrocarbon LID threshold was observed on the $10^o$ off-axis sample. On the other hand, the minimum average LID threshold value and variation in the LID threshold value of water and hydrocarbons were observed for $15^o$ off-axis sample. (100) $CaF_2$ has medium variation of LID threshold for both water and hydrocarbons. Also its average LID threshold for both water and hydrocarbons falls between that of $10^o$ and $15^o$ off-axis samples. As it is assumed that contaminants are preferentially adsorbed at surface defects, the variation of LID thresholds would reflect the difference between defect structures of the surfaces. A large variation of LID thresholds may suggest a large variation in defects existing on the surface while a smaller variation may suggest more uniformity in defects. In the experiments conducted on $15^o$ off-axis (100) $CaF_2$ samples, m/z = 59 and 137 values attributed to fragments of $CaF_2$ compound were observed occasionally. The least average LID threshold value of $15^o$ off-axis (100) $CaF_2$ samples suggests that they are more readily damaged at higher fluences compared to (100) and $10^o$ off-axis (100) $CaF_2$ samples.

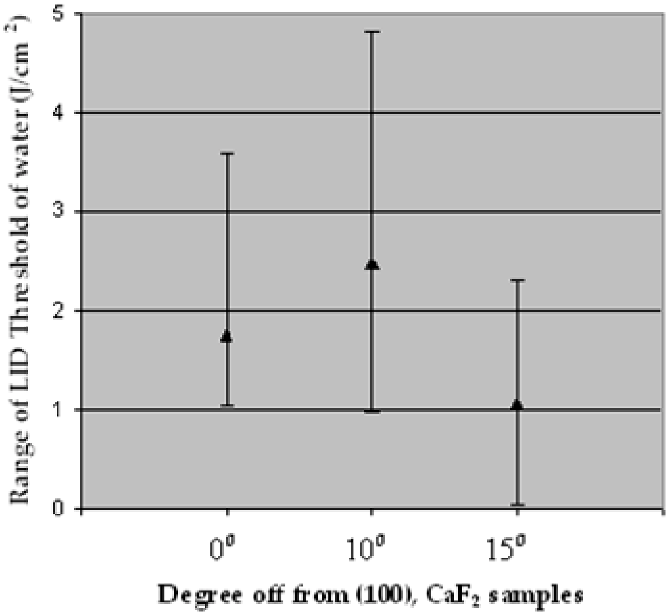

Figure 4.8. Variation of LID threshold of water on different off-axis (100) $CaF_2$ surface

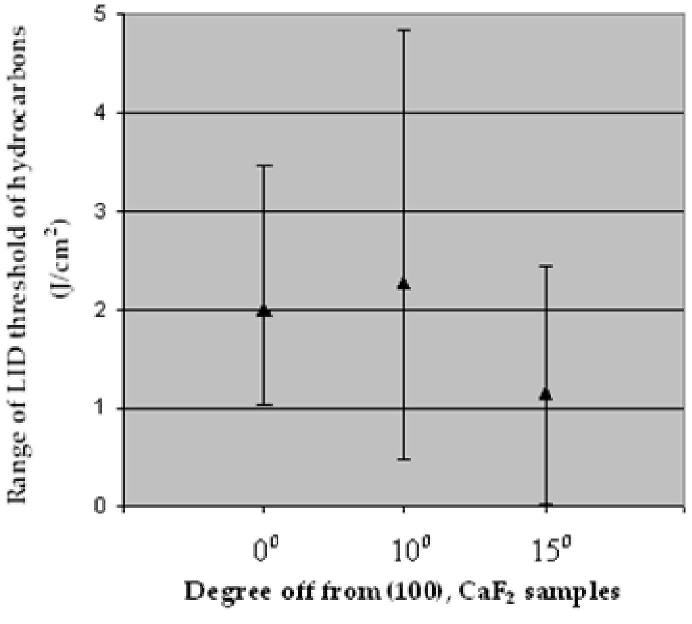

Figure 4.9. Variation of LID Threshold of hydrocarbons on different off-axis (100) $CaF_2$ surface

## 4.5. LID fluence of different samples:

Comparison plots of LID fluence of water and hydrocarbons from (100), 10 and 15 off-axis (100) $CaF_2$ surface are given in Figures 4.10 and 4.11 respectively. The LID fluence plots also show range by bars and average value by arrow on bar, of desorbed water and hydrocarbons fluence with each sample. As seen from the following plots, the $10^o$ off-axis sample has the highest and $15^o$ off-axis sample has the lowest average LID fluence and variation of LID fluence for water and hydrocarbon. The (100) $CaF_2$ has medium average value of LID fluence and variation of LID fluence of water and hydrocarbons. As it is assumed that contaminants are preferentially adsorbed at surface defects, more LID fluence suggests the existence of more surface defects or few larger surface defects. A greater range of desorption fluence implies non-uniformity of defect size or type of surface defects.

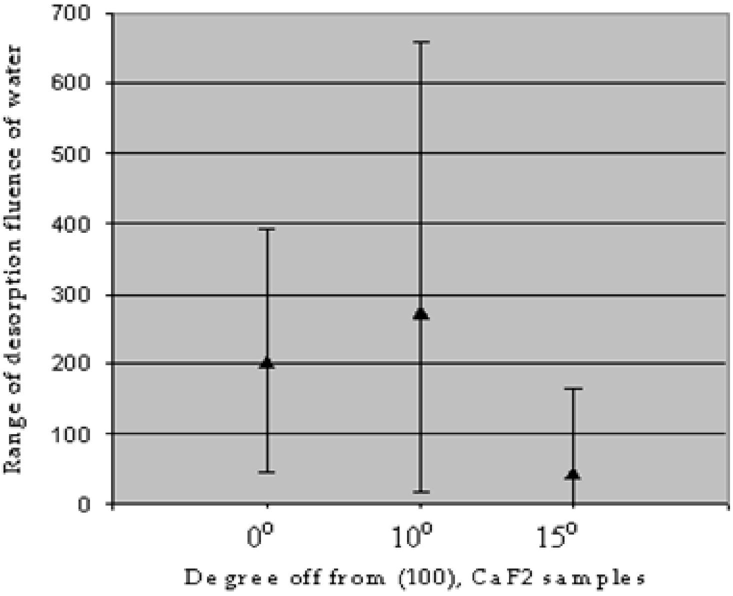

Figure 4.10. LID fluence of water from different off-axis (100) $CaF_2$ surface

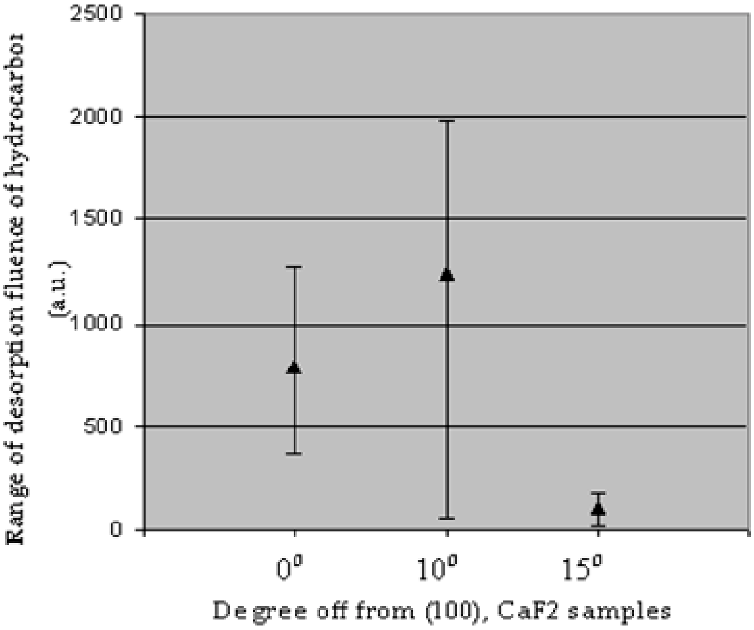

Figure 4.11. LID fluence of hydrocarbons from different off-axis (100) $CaF_2$ surface

## 4.6. Surface mapping:

In order to obtain surface maps of a sample, first the desorption threshold energy densities at various randomly selected sites were determined using the N ($\phi_0$)/1 technique. Desorption in mapping experiments was obtained by using a single laser energy density at all sites. The laser energy density chosen to perform mapping experiments was a little higher (10 %) than the highest threshold energy density obtained from the N ($\phi_0$)/1 experiment. Five nominally identical laser pulses were used to irradiate each site on the sample. A high desorption fluence was observed at areas closer to the edge, as more defects exist at the edge resulting from cutting and polishing of the sample. Thus, it was assumed that areas away from the edge represent the surface characteristics of the sample. Therefore, all the mapping experiments were performed within 4 x 5 mm area in the center of the 12 mm diameter samples.

Maps of LID water and hydrocarbon ions, from a polished (100) $CaF_2$ surface are given in Figure 4.12. A laser energy density of 4.42 J/cm$^2$ was used in order to obtain desorption from various sites. The separation between two sites was 500 μm, both horizontally and vertically. As seen from the 3D plots, the maximum total desorption fluence of water obtained was ≈ 450 whereas for hydrocarbons it was ≈ 1200.

A contour map of water and hydrocarbons desorption fluence from (100) $CaF_2$ is shown in Figure 4.13. This figure clearly shows that both water and hydrocarbons have similar spatial distribution at almost all the sites. Also, it can be seen that water and hydrocarbon local concentration maxima occurred at the same location on almost all the sites with only a few exceptions. The reason for co-existence and occurrence of local maximum at a same location could be due to water and hydrocarbons being co-adsorbed into surface defects during the polishing and cleaning processes.

For the 10$^o$ degree off-axis (100) $CaF_2$ surface, the laser energy used to conduct surface mapping was 4.94 J/cm$^2$. The separation between two sites was 500 μm in both horizontal and vertical directions. Figure 4.14 shows the 3-D surface maps of water and hydrocarbons on the 10$^o$ degree off-axis (100) $CaF_2$ surface. The maximum total desorption fluence of water and hydrocarbons obtained were ≈ 900 and ≈ 3200 respectively. From the contour map of water and hydrocarbons shown in Figure 4.15, it can be seen that water and hydrocarbons on 10$^o$ degree off-axis (100) $CaF_2$ surface also have similar spatial distributions. The local concentration maximum for both water and hydrocarbons occurred at the same location with few exceptions.

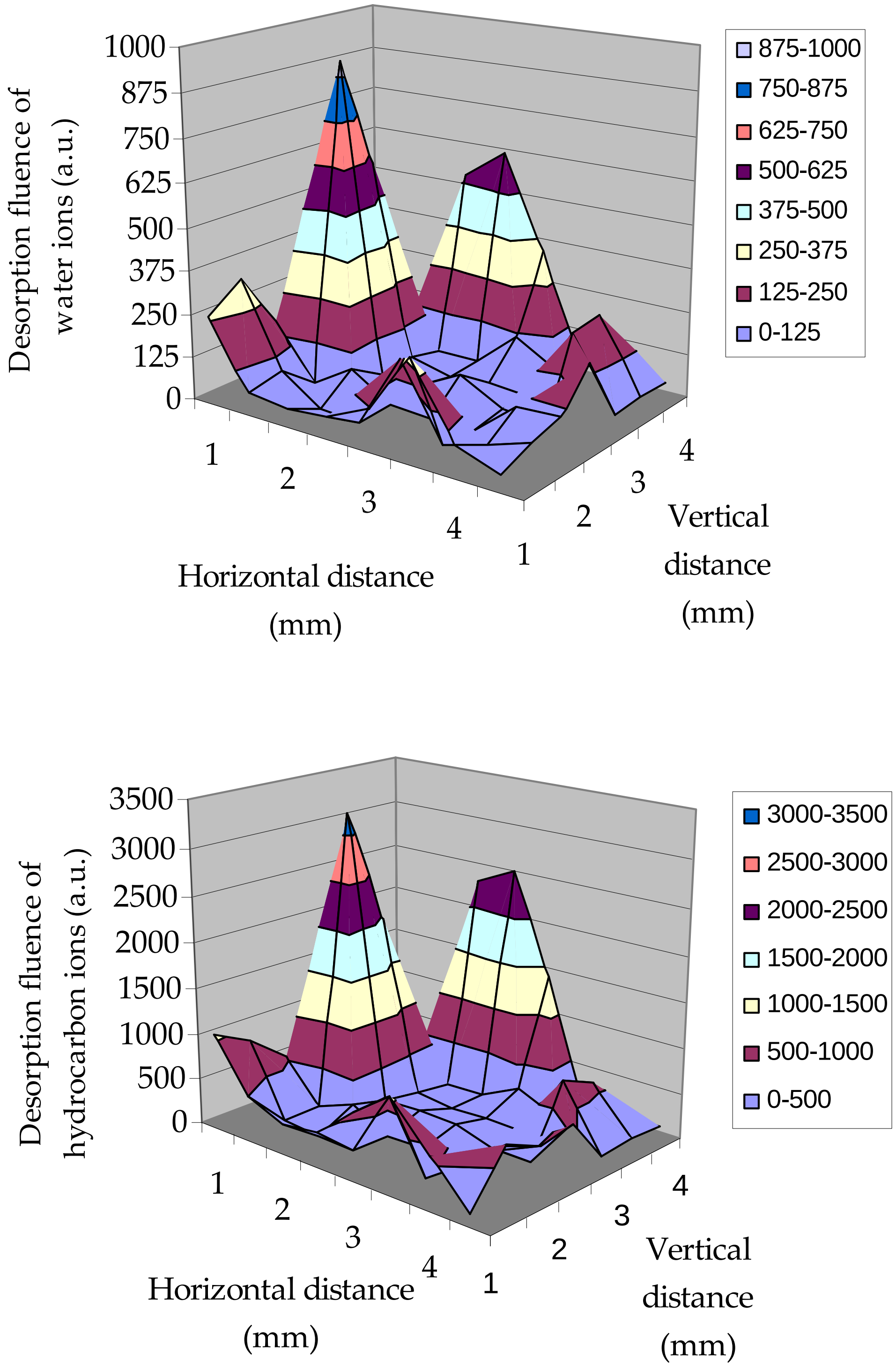

Figure 4.12. Surface maps of water and hydrocarbons on a super polished (100) $CaF_2$ sample

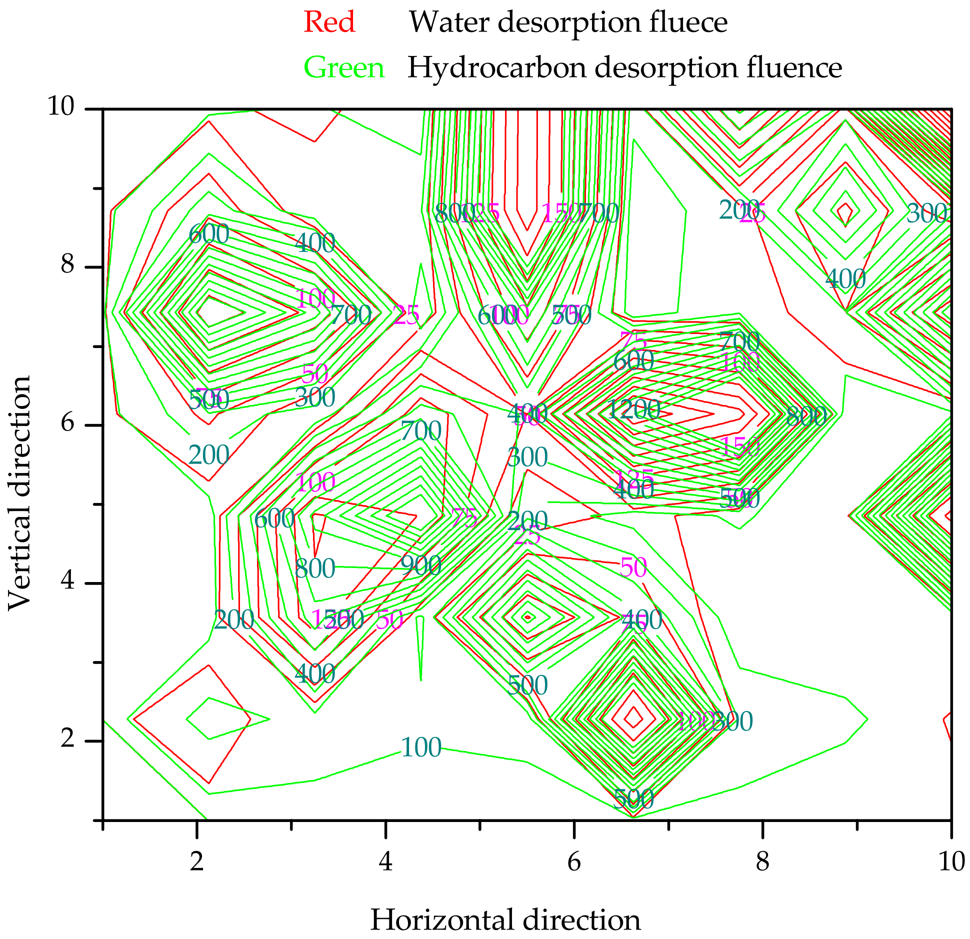

Figure 4.13. Surface map of both water and hydrocarbons on a super polished (100) $CaF_2$ surface

For the 15° off-axis $CaF_2$ sample, the 3-D surface maps of water and hydrocarbons are given in Figure 4.16. A laser energy density of ≈ 2.4 J/cm$^2$ was used to desorb the contaminants. The highest LID threshold value observed for this 15° off-axis $CaF_2$ sample was only ≈ 2.4 J/cm$^2$. The spacing between any two sites was maintained at 300 μm. Less spacing was used on this sample compared to (100) and 10° off-axis (100) $CaF_2$ sample as area irradiated by a laser beam is directly proportional to energy density of the laser beam.

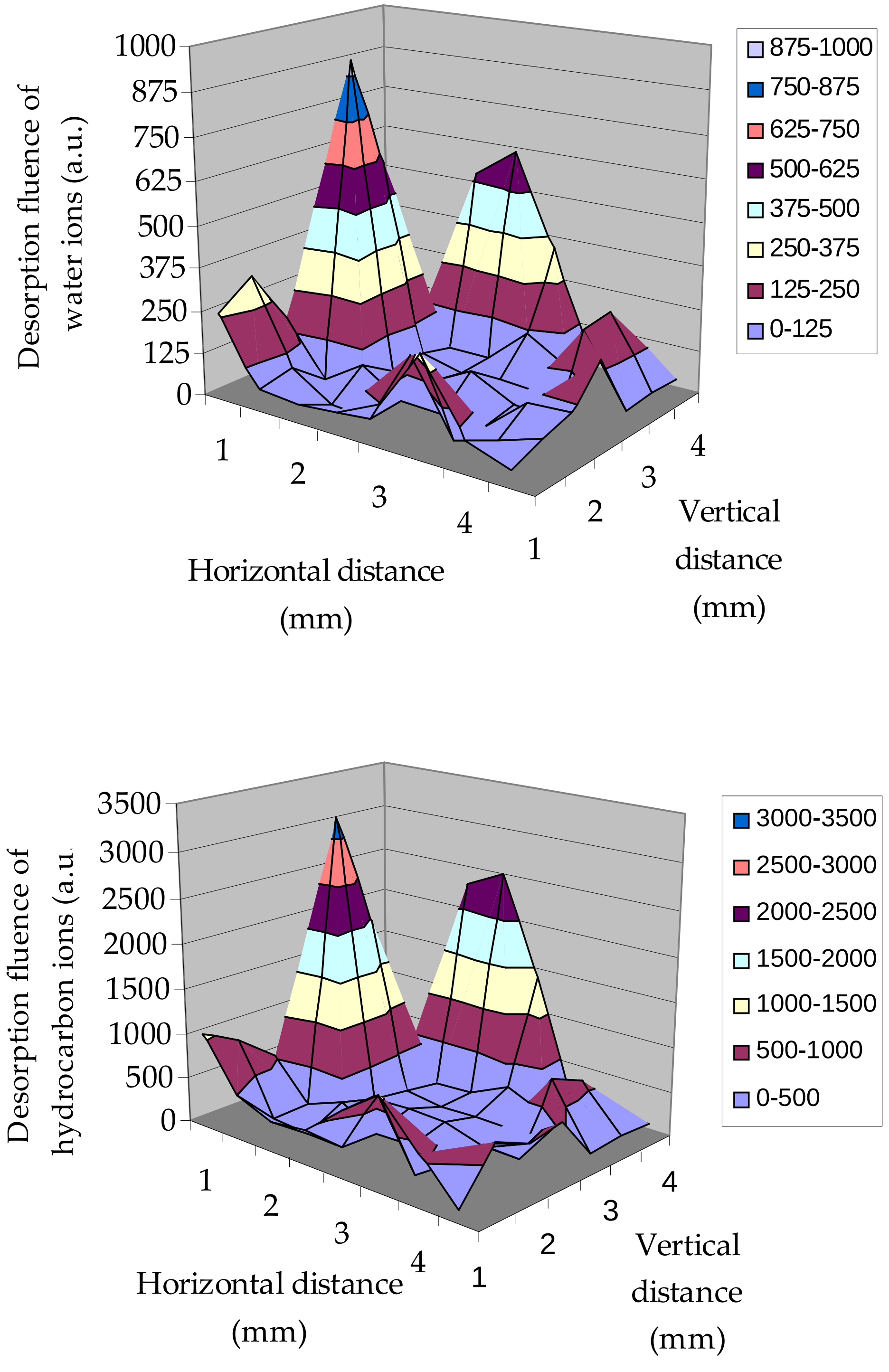

Figure 4.14. Surface maps of water and hydrocarbons on a super polished 10$^{o}$ off-axis (100) $CaF_2$ sample

The maximum total LID fluence observed for water and hydrocarbons were ≈ 290 and ≈ 1140 respectively. Less desorption fluence was observed as less energy density was used to do surface mapping of this sample. For the 15° off-axis sample water and hydrocarbons also had similar spatial distribution with their local concentration maximum appearing at the same location as shown in Figure 4.17.

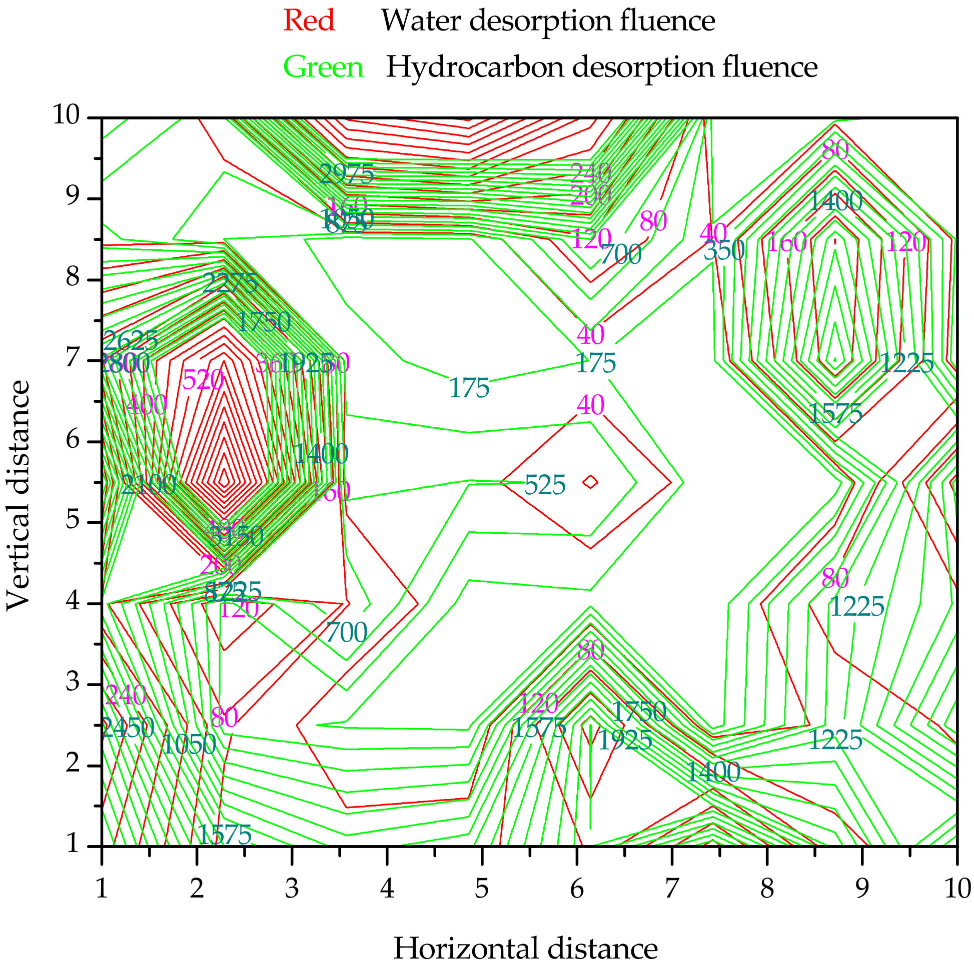

Figure 4.15. Surface map of both water and hydrocarbons on a super polished 10° off-axis (100) $CaF_2$ sample

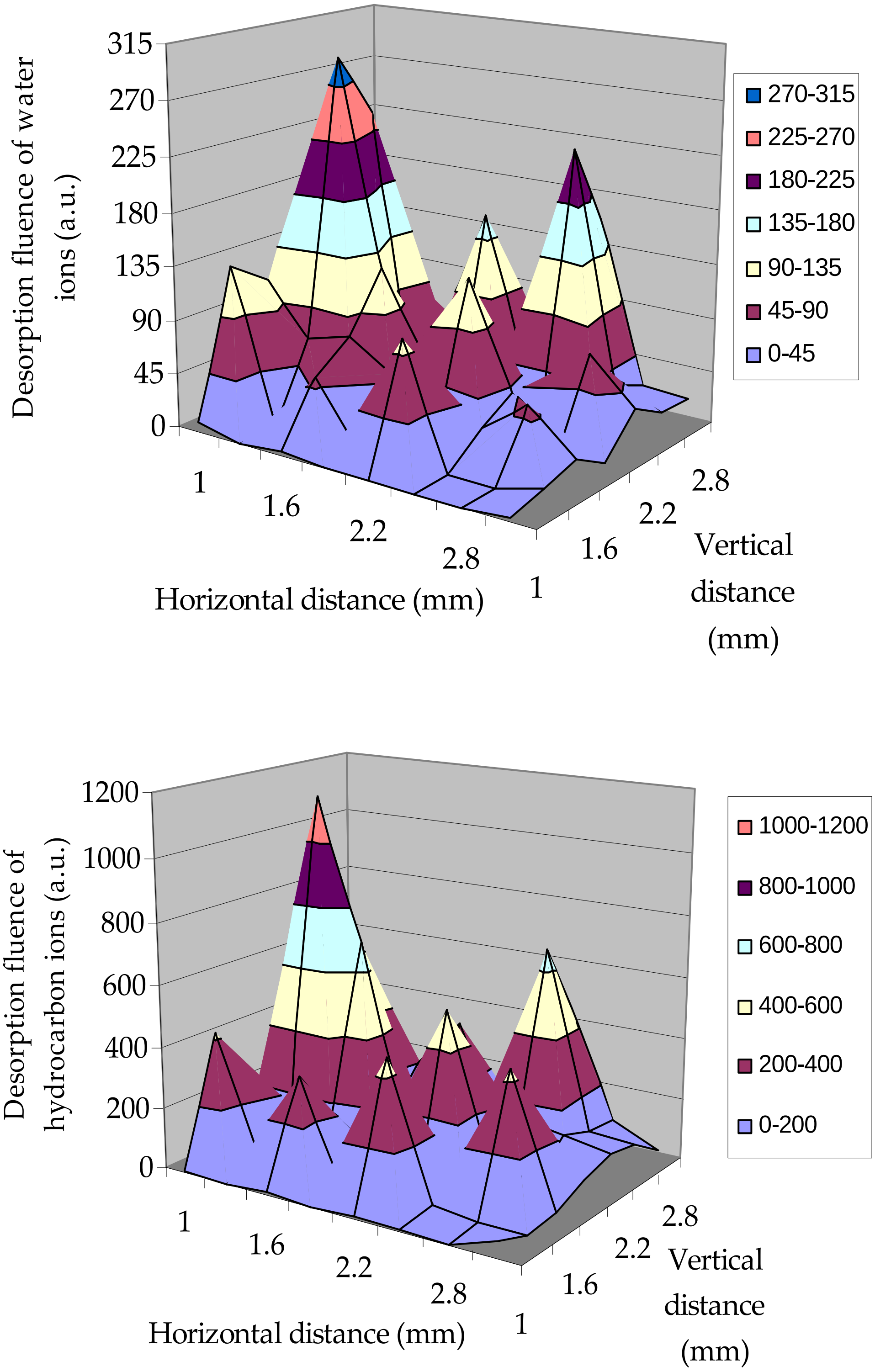

Figure 4.16. Maps of water and hydrocarbons on a super polished 15$^{\circ}$ off-axis (100) $CaF_2$ sample

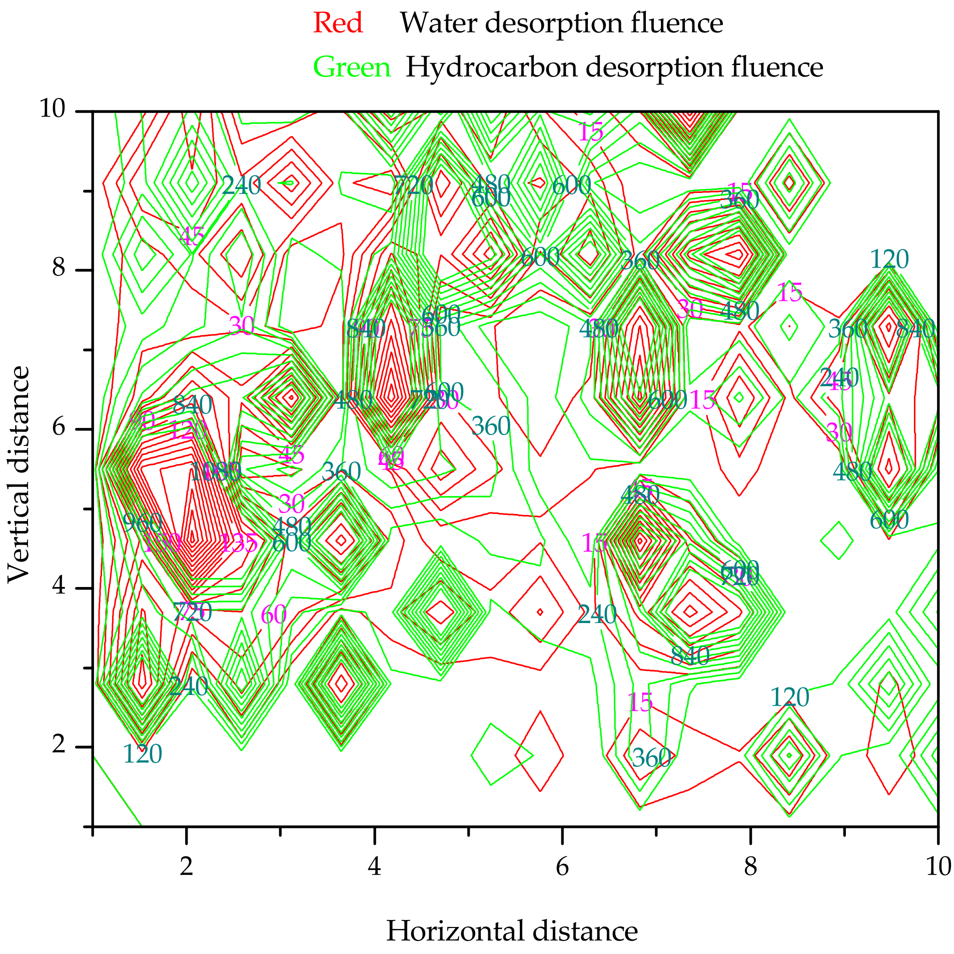

Figure 4.17. Surface map of both water and hydrocarbons on a super polished 15$^o$ off-axis (100) $CaF_2$ sample

Surface maps of water and hydrocarbons on (111) $CaF_2$ sample are given in Figures 4.18. The laser energy density used to conduct surface map experiment on this sample was 4.5 J/cm$^2$. The spacing between any two sites was maintained at 500 µm. The global maximum of LID water fluence and hydrocarbon fluence are ≈ 94 and ≈ 755 respectively.

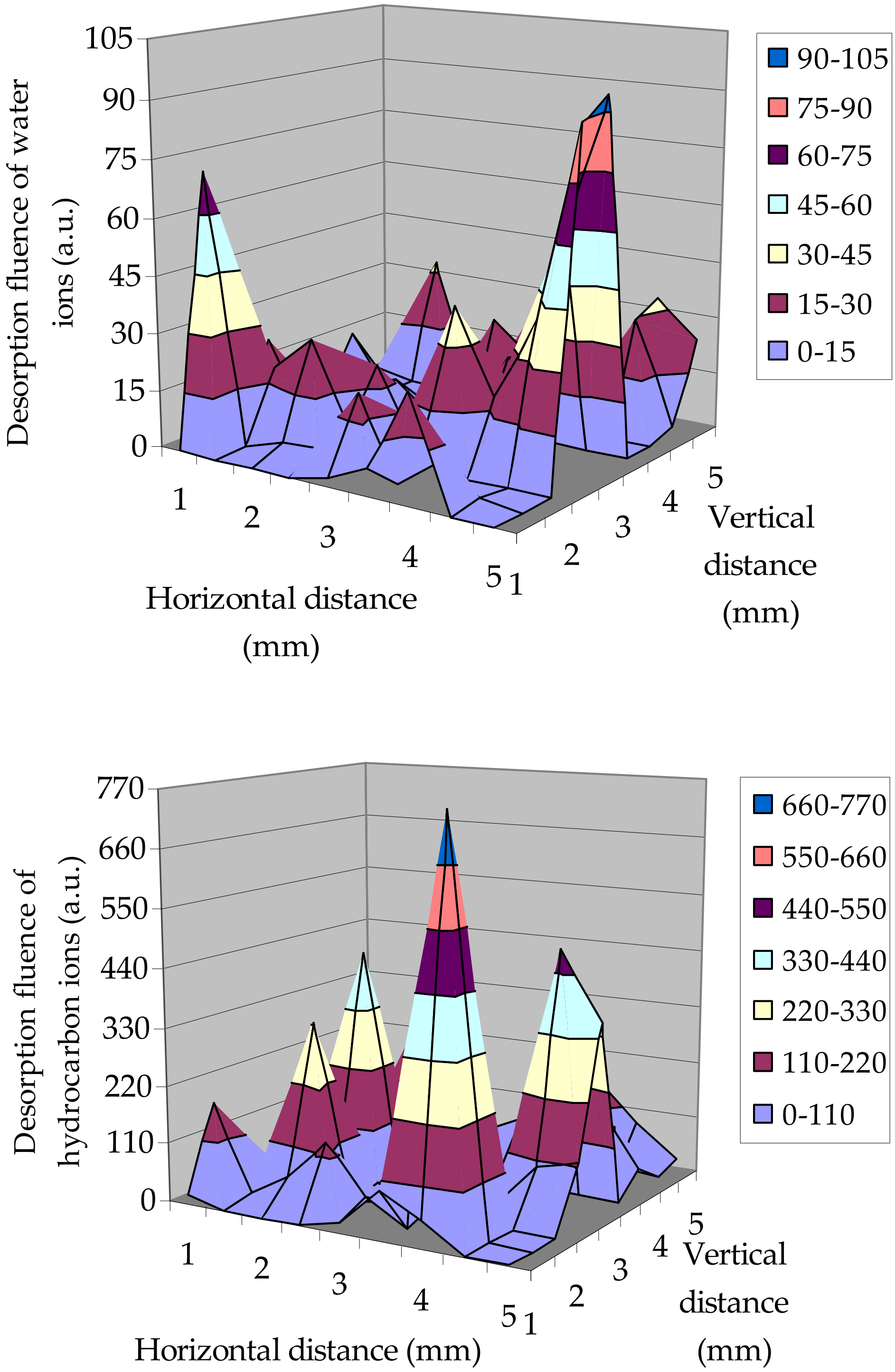

Figure 4.18. Maps of water and hydrocarbons on a (111) $CaF_2$ sample

The contour map of the surface maps of both water and hydrocarbons is given in Figure 4.19. As seen from the Figures 4.18 and 4.19, the water and hydrocarbons on (111) $CaF_2$ sample also have similar distribution at most of the sites with their local concentration maximum occurring at same location for most of the sites. An obvious difference observed between (100) and (111) CaF2 samples is that the global maximum of water and hydrocarbons on (111) did not occur at same location where as they did occur at same location on all (100) (i.e., (100), 10° and 15° off-axis (100)) $CaF_2$ samples.

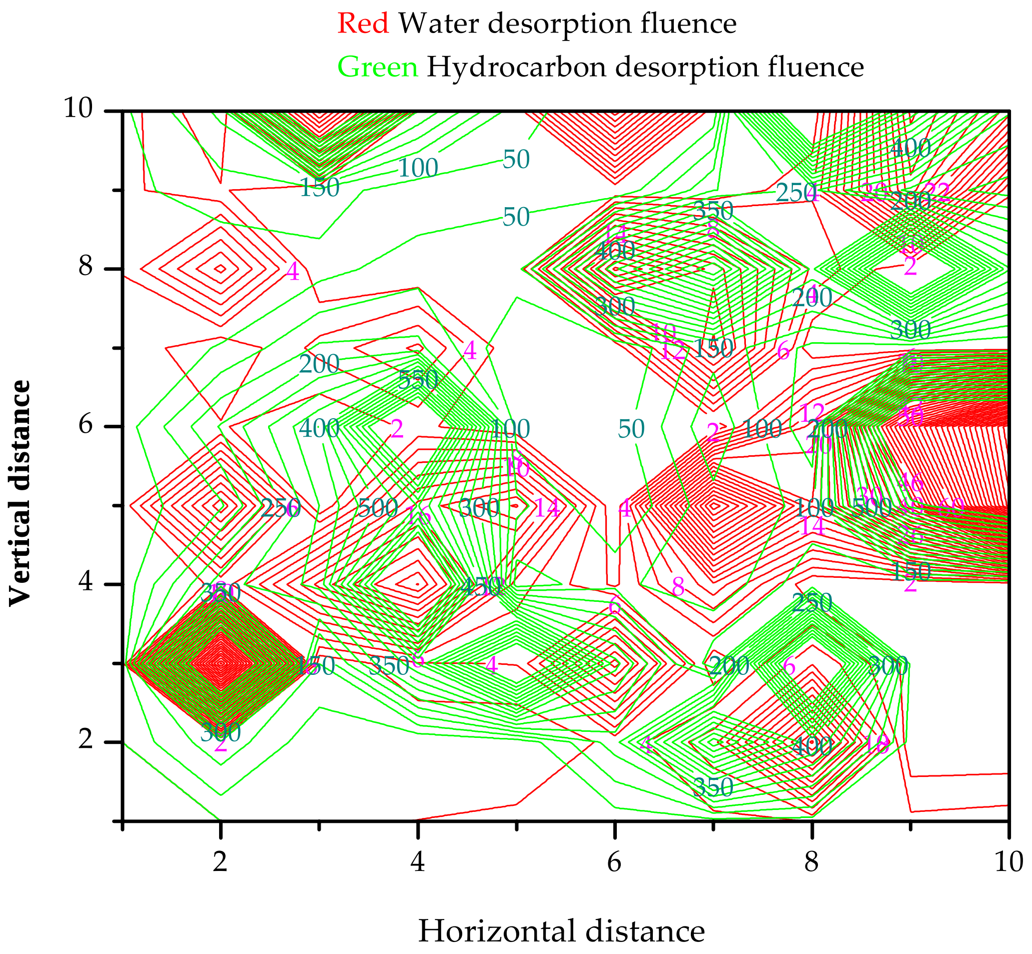

Figure 4.19. Surface map of both water and hydrocarbons on a (111) $CaF_2$ sample

## 4.7. Surface roughness:

Surface topography and roughness of the samples were determined by numerous AFM scans. Scan sizes of 20 µm x 20 µm, 10 µm x 10 µm and 5 µm x 5 µm were performed. Figure 4.20 shows the surface topography of (100) $CaF_2$. The color bar on to the right hand side of the scan gives the color scale of the scan. As seen from the figure lines of different depth and width caused by polishing are scattered over the surface. The depth and width of a line can be obtained by performing sectional analysis of the line. For example, in Figure 4.21 the depth (given by red markers) and the width (given by green markers) of the marked line were 1.39 nm and 0.9 µm respectively. $R_{rms}$ and $R_{ave}$ at this scan area (site 1) were 0.48 nm and 0.372 nm respectively. Figure 4.22 shows an AFM scan of (100) $CaF_2$ surface at a different site. The AFM scan at this site showed some particles along with lines due to polishing. $R_{rms}$ and $R_{ave}$ at this scan area were 0.5 nm and 0.37 nm respectively. The range of $R_{rms}$ values observed on the (100) $CaF_2$ sample was from ≈ 0.2nm to ≈ 0.6 nm.

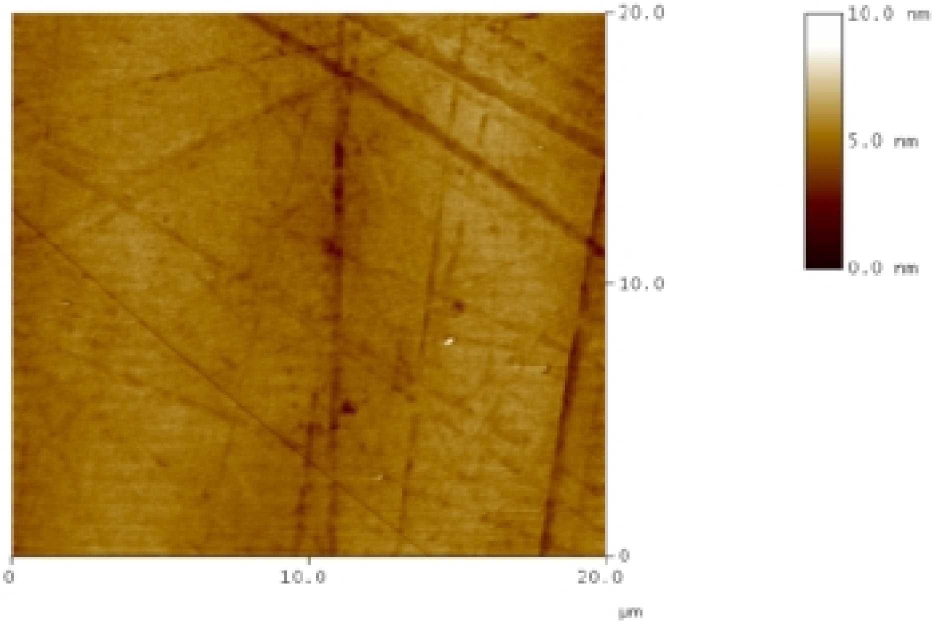

Figure 4.20. AFM scan of (100) $CaF_2$ surface at site 1

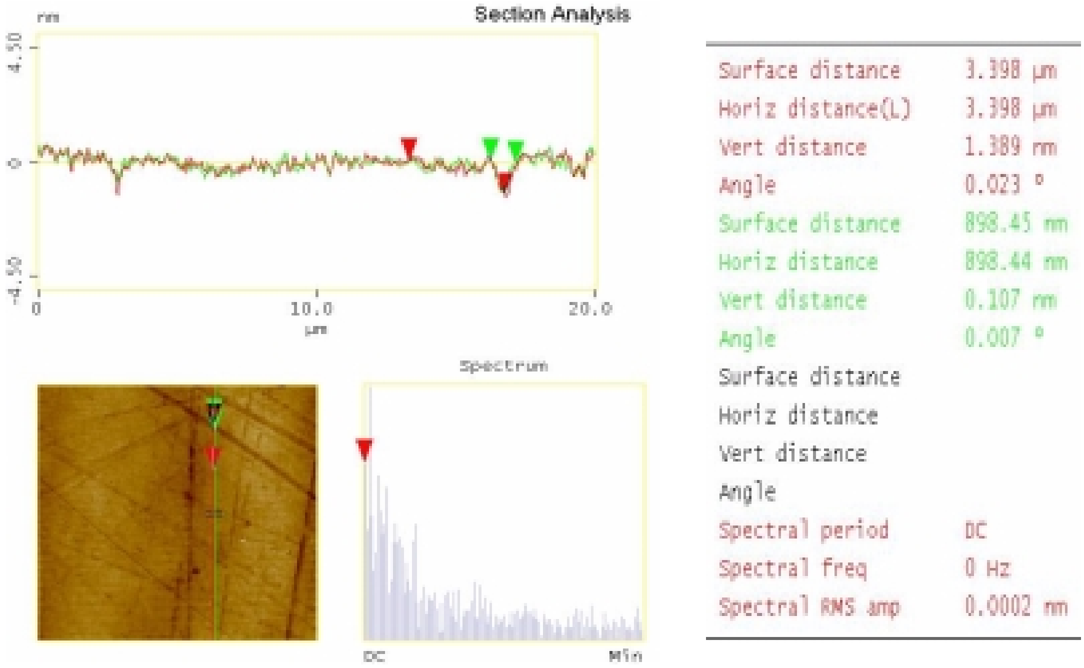

| | |
|---|---|
| Surface distance | 3.398 µm |
| Horiz distance(L) | 3.398 µm |
| Vert distance | 1.389 nm |
| Angle | 0.023 ° |
| Surface distance | 898.45 nm |
| Horiz distance | 898.44 nm |
| Vert distance | 0.107 nm |
| Angle | 0.007 ° |
| Surface distance | |
| Horiz distance | |
| Vert distance | |
| Angle | |
| Spectral period | DC |
| Spectral freq | 0 Hz |
| Spectral RMS amp | 0.0002 nm |

Figure 4.21. Sectional analysis on (100) $CaF_2$ sample surface

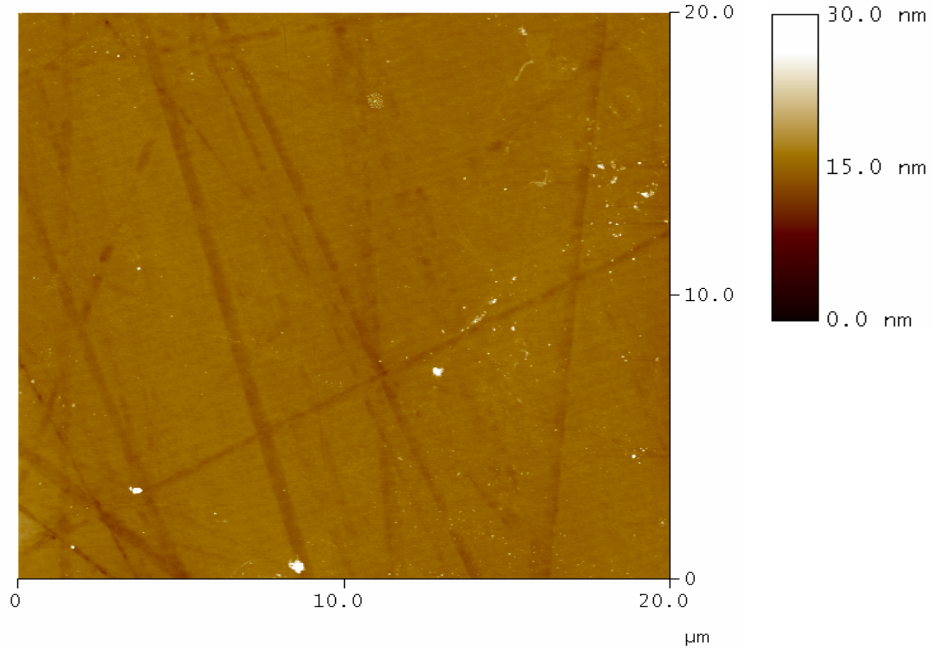

Figure 4.22. AFM scan of (100) $CaF_2$ at site 2

A 10 µm x 10 µm AFM scan of the 10° off-axis (100) $CaF_2$ surface is given in Figure 4.23. $R_{rms}$ and $R_{ave}$ at this site were ≈ 0.34 nm and ≈ 0.21 nm. As with (100) $CaF_2$ surface, the 10° off-axis (100) $CaF_2$ surface also showed randomly spaced polishing lines and particles. The dark spot in the scan is a pit on the surface. The Rrms values observed on this sample varied from ≈ 0.25 nm to ≈ 0.68 nm.

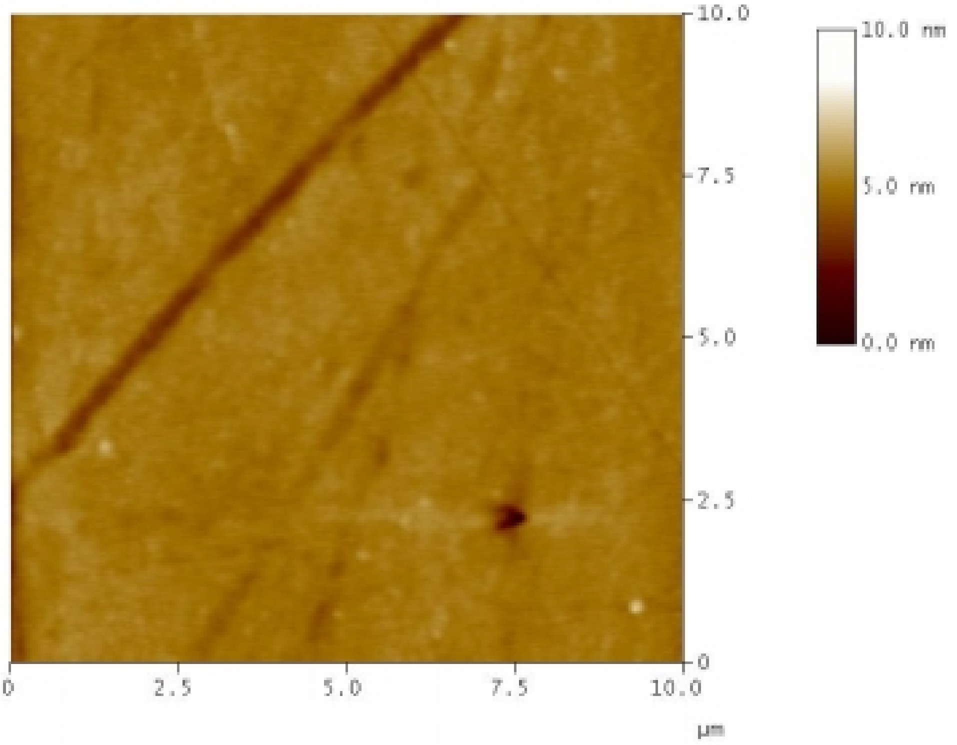

Figure 4.23. 10° off-axis (100) $CaF_2$ surface

Figure 4.24 shows a 20 µm x 20 µm AFM scan of the 15° off-axis (100) $CaF_2$ surface. $R_{rms}$ and $R_{ave}$ of this scan were 0.3 nm and 0.18 nm respectively. This 15° off-axis (100) $CaF_2$ sample showed fewer polishing lines compared to other 15° off-axis (100), 10° off-axis (100) and (100) samples. The range of Rrms values observed for 15° off-axis (100) $CaF_2$ was from ≈ 0.3 nm to ≈ 0.75 nm.

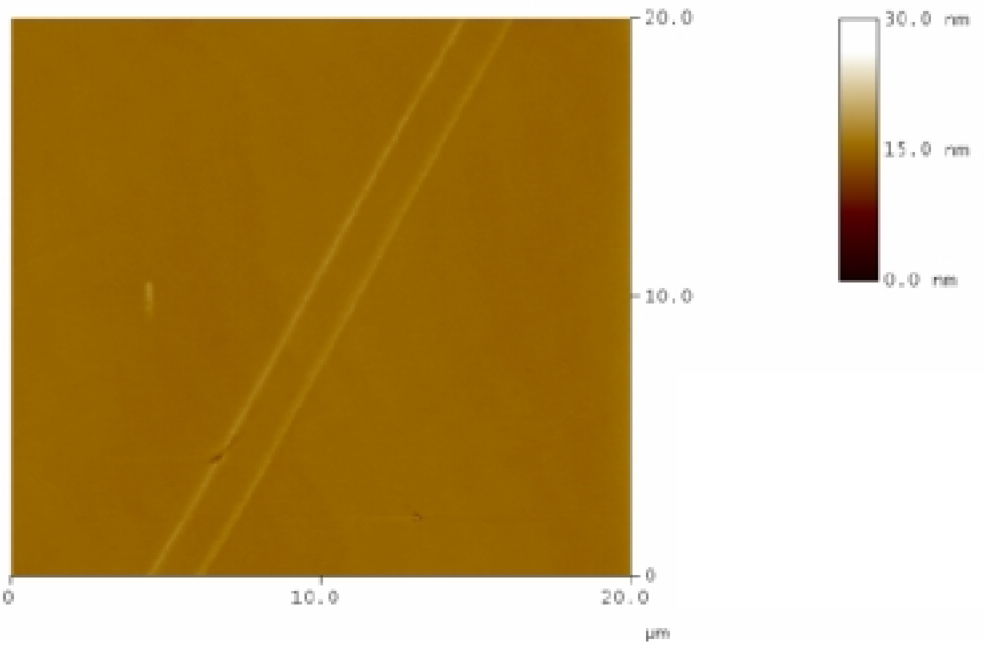

Figure 4.24. 15° off-axis (100) $CaF_2$ surface

The maximum values of depth and width of polishing lines on the samples observed were ≈ 1 µm and ≈ 3 nm respectively. Scans of 20 µm x 20 µm were performed at consecutive sites (area of 60 µm x 60 µm), on (100) and 15° off-axis (100) $CaF_2$ samples, using the autoscan feature of AFM. The scans showed relatively less variation of measured roughness values for 15° off-axis (100) $CaF_2$ compared to (100) $CaF_2$. The AFM scans did not show strong relationship between roughness values on a sample and LID fluence from the sample.

# CHAPTER 5

# CONCLUSIONS

Contamination of optical elements has always been a serious problem in semiconductor industry's IC manufacturing process. With minimum feature size approaching 70 nm (157nm lithography process) even a little surface contamination (like molecular contamination) of optical elements distorts the image produced by stepper tools and adversely affects the wafer yield. Thus understanding the types of contaminants and their distribution on optical surfaces at 157 nm is critical. In this study, adsorbed surface contaminants on the candidate optic material for DUV optical lithography ($CaF_2$) were analyzed. The data reported here can be used in modifying the conventional processing to produce cleaner optical surfaces with the required figure or designing an efficient in situ cleaning process for optical elements. The different samples analyzed include (111), (100), 10° and 15° off-axis (100) $CaF_2$ samples. Water, hydrocarbons, oxygen-containing hydrocarbons and alkali metal ions were detected on all the sample surfaces.

Desorption threshold energy densities of water and hydrocarbon ions at various sites on the samples were determined using a degenerate threshold model modified for the elliptical Gaussian cross sectional beam produced on the sample. The values of desorption threshold energy densities observed for water at 2.94 μm (for example, 0.6 J/cm$^2$ and 2.2 J/cm$^2$) are one order of magnitude lower than the desorption thresholds reported at 2.7 μm (for example, 4.7 J/cm$^2$ and 23 J/cm$^2$).[31] This difference is consistent with the fact that the absorption coefficient of water at 2.94 μm ($\alpha_{2.94\mu m} = 1.22 \times 10^4$ cm$^{-1}$) is one order of magnitude higher than at 2.7 μm ($\alpha_{2.7\mu m} = 0.74 \times 10^3$ cm$^{-1}$).[5] Therefore, higher cleaning efficiency for highly transmissive optical surfaces was demonstrated by using a wavelength that is strongly absorbed by adsorbed surface contaminants. From the experimental data, no direct relationship between threshold energy density and desorption fluence was observed. The threshold energy density at a particular site is assumed to be independent of desorption fluence and is assumed to depend only on local concentration of adsorbates.

Surface maps of water and hydrocarbon desorption fluence on the samples were plotted. Surface maps showed that water and hydrocarbons co-existed at all the sites where they were observed. Water and hydrocarbons seem to have similar distributions, with their local maximum concentration occurring at the same locations on (100) $CaF_2$ samples. From the surface maps, it was also observed that the desorption fluence was higher at edges, suggesting the presence of more surface defects near edges.

A comparison of desorption fluence for the samples showed that the maximum, medium and minimum mean desorption fluence were observed for 10° off-axis (100), (100) and 15° off-axis (100) $CaF_2$ samples respectively. The 10° off-axis (100) $CaF_2$ samples are assumed to have more or bigger surface defects compared to (100) and 15° off-axis (100) $CaF_2$ samples. Also, the desorption fluence variation was higher for the 10° off-axis (100) $CaF_2$ sample compared to the other two. It is concluded that, among the samples investigated, the 10° off-axis (100) $CaF_2$ sample has more non-uniformly distributed surface defects. It was observed that 15° off-axis (100) $CaF_2$ samples have lower damage thresholds and readily damage at higher laser fluences. Finally, surface topography of the samples observed by AFM showed polishing scratches and some particles on the surface of the samples. No strong relationship between measured roughness and LID fluence of water and hydrocarbons was observed from AFM scans.

## 5.1. Scope for future work:

There are many possibilities for future work in this area. With the surface adsorbate and their distribution on $CaF_2$ sample reported, either the conventional processing has to be modified or an efficient cleaning system has to be developed to clean molecular contamination from optical surfaces in situ. Temperature calculations that give more insight into how the substrate is heated and how far the heat is being transferred on/into the surface during laser cleaning have to be performed.

Surface maps of water and hydrocarbons on (111) $CaF_2$ sample also showed that water and hydrocarbons were co-adsorbed at defect sites. The (111) $CaF_2$ sample also has similar distribution of water and hydrocarbons with their local concentration maximum occurring at the same location. The major difference observed for (111) $CaF_2$ sample from (100) $CaF_2$ sample is that (111) orientation sample does not have global maximum desorption fluence of water at a site that has global maximum hydrocarbon desorption fluence and vice versa. The similarities and differences between (111) and (100) should be investigated thoroughly as a combination of these two orientation $CaF_2$ samples is going to be used in the VUV optical lithography tools currently under development to reduce the intrinsic birefringence of $CaF_2$.

Also further research can be done to distinguish the different types of defects on optical surfaces. Understanding the different types of surface defects helps in producing optical materials with less number of surface defects. Similarly, further investigation should be pursued in the area of surface characterization of different orientation optical surfaces to better understand the reason for an increase/decrease in surface roughness value and the correlation between surface nanotopography and adsorbed contaminants.

# REFERENCES

1. L. W. Liebmann, S. M. Mansfield, A. K. Wong, M. A. Lavin, W. C. Leipoid and T. G. Dunham, “TCAD Development for Lithography Resolution enhancement”. IBM Journal of Research and Development, 45/5, 651-665, 2001.

2. Daniel C. McCarthy, “Phase-Shift Techniques Rewrite the Semiconductor Road Map”. Photonics Spectra, 76-81, December, 2001.

3. G. E. Moore, “Cramming More Components onto Integrated Circuits”. Electronics, 38/8, April 19, 1965.

4. V. Liberman, T. M. Bloomstein, M. Rothschild, J. H. C. Seblacek, R. S. Uttaro, A. K. Bates, C. Van Peski and K. Orvek, “Material Issues for Optical Components and photomasks in 157nm lithography”. Journal of Vacuum Science and Technology B, 17, 3273- 3279, 1999.

5. J. H. Burnett, Z. H. Levine and E. L. Shirley, “Intrinsic Birefringence in Calcium Fluoride and Barium Fluoride”. Physical Review B, 64, 241102 (R), 1-4, 2001.

6. “SEMATECH Reports 157nm Lithography Progress”. www.e-insite.net/esec/Article_217545.htm, Online staff – Electronic News, 05-15-2002.

7. H. Johansen and G. Kastner, “Surface Quality and Laser-Damage Behaviour of Chemo-Mechanically Polished $CaF_2$ Single Crystals Characterized by Scanning Electron Microscopy”. Journal of Materials Science, 33, 3839-3848, 1998.

8. M. R. Querry, D. M. Wieliczka and D. J. Segelstein, “Handbook of Optical Constants of Solids II”. Edited by E.D. Palik Academic, San Diego, CA, 1059-1077, 1991.

9. T. M. Bloomstein, V. Liberman, M. Rothschild, S. T. Palmacci, D. E. Hardy and J. H. C. Sedlacek, “Contamination Rates of Optical Surfaces at 157nm in the Presence of Hydrocarbon Impurities”. Optical Microlithography XV, Proceedings of SPIE, 4691, 709-723, 2002.

10. E. Eva, K. Mann, N. Kaiser, B. Anton, R. Henking, D. Ristau, P. Weissbrodt, D. Mademann, L. Raupach, E. Hacker, “Laser Conditioning of $LaF_3$ $MgF_2$ Dielectric Coatings at 248nm”. Applied Optics-OT, 35/28, 5613-5619, 1996.

11. C. Gorling, U. Leinhos and K. Mann, “Comparative Studies of Absorptance Behaviour of Alkaline-Earth Fluorides at 193nm and 157nm”. Applied Physics B, 74, 259-265, 2002.

12. T. M. Bloomstein, M. Rothschild, R. R. Kunz, D. E. Hardy, R. B. Goodman and S. T. Palmacci, “Critical Issues in 157nm Lithography”. Journal of Vacuum Science and Technology B, 16-6, 3154-3157, 1998.

13. R. J. Cotter, “Time-of-Flight Mass Spectrometry: Instrumentation and Applications in Biological Research”. The American Chemical Society, Chapter 1 and 2, 1-45, 1997.

14. M. L. Pacholshi and N. Winograd, “Imaging with Mass Spectroscopy”. Chemical Reviews, 99/10, 2977-3005, 1999.

15. K. D. James and B. A. Dawn, “Quantification of Topographic Structure by Scanning Probe Microscopy”. Journal of Vacuum Science and Technology B, 15-4, 1483-1493, 1997.

16. S. R. Rebecca, S. Robert and S. P. Vincent, “Effect of Surface Quality on Transmission Performance for (111) $CaF_2$”. Applied Surface Science, 264-269, 2001.

17. D. Angela, K. Igor, G. Stefan, S. Jorg and N. Gunther, “Surface Characterization of Optical Components for the DUV, VUV and EUV”. Microelectronic Engineering, 57/58, 65-70, 2001.

18. M. Niwa, H. Iwasaki, Y. Watanabe, I. Sumita, N. Akutsu and Y. Akutsu, “Statistical Properties of Atomic-Scale $Si/SiO_2$ Interface Roughness Studied by STM”. Applied Surface Science, 60/61, 39-44, 1992.

19. Digital Instruments Scanning Probe Microscopy Training Manual, page7.

20. L. P. Levine, J. F. Ready and G. E. Bernal, “Gas Desorption produced by Giant Pulse Laser”. Journal of Applied Physics, 38, 331-336, 1967.

21. S. M. Bedair, H. P. SmithJr., “Atomically Clean Surfaces by Pulsed Laser Bombardment”. Journal of Applied Physics, 40/12, 4776-4781, 1969.

22. H. F. Winters and E. J. Kay, “Gas Analysis in Films by Laser-Induced Flash Evaporation Followed by Mass Spectrometry”. Journal of Applied Physics, 43/3, 789-793, 1972.

23. T. J. Chuang, “Infrared Laser Induced reaction of $SF_6$ with Silicon Surfaces”. Journal of Chemical Physics, 72/11, 6303-6304, 1980.

24. W. Zapka, W. Ziemlich, A. C. Tam, “Efficient Plused Laser Removal of 0.2 µm Sized Particles from a Solid Surface”. Applied Physics Letter, 58/20, 2217-2219, 1991.

25. N. S McIntyre, R. D. Davidson, T. L. Walzak, R. Williston, M. Westcott, A. Pekarshy, “Uses of Ultraviolet/Ozone for Hydrocarbon Removal: Applications to surfaces of Complex Composition or Geometry”. Journal of Vacuum Science and Technology A, 9, 1355, 1991.

26. A. Bodemann, N. Kaiser, L. Raupach, P. Weissbrodt, E. Hacker, “248-nm Laser - Interaction Studies on $MgF_2$/$LaF_3$ Optical Coatings by Mass Spectroscopy and X-ray Photoelectron Spectroscopy”. Proceedings SPIE 2714, 405-415, 1995.

27. K. Yamaguchi, Y. Uematsu, Y. Ikoma, F. Watanabe, T. Motooka, T. Igarashi, “Thermal Desorption Spectroscopy and Molecular Beam Time-of-Flight Studies of Silicon Water Ultraviolet/Ozone Cleaning”. Journal of Vacuum Science and Technology B, 15, 277-281, 1997.

28. S. Boughaba, X. Wu, E. Sacher and M. Meunier. Journal of Adhesion, 61, 293, 1997.

29. J. C. Lu, Y. S. Li and X. F. Zong. Journal of Electron Manufacturing, 8, 173, 1998.

30. S. J. Lee, K. Imen and S. D. Allen, “Laser-Assisted Particle Removal from Silicon Surfaces”. Microelectronic Engineering, 20, 145-157, 1993.

31. S. D. Allen, J. O. Porteus and W. N. Faith, “Infrared Laser-Induced Desorption of $H_20$ and Hydrocarbons from Optical Surfaces”. Applied Physics Letters, 41/5, 416-418, 1982.

32. D. J. Krajnovich, M. Kulkarni, W. P. Leung, A. C. Tam, A. Spool, B. York, “Testing of the Durability of Single-Crystal Calcium Fluoride with and without Antireflection Coatings for use with High-Power KrF Excimer Lasers”. Applied Optics-OT, 31-28, 6062-6106, 1992.

33. T. M. Bloomstein, M. Rothschild, R. R. Kunz, D. E. Hardy, R. B. Goodman and S. T. Palmacci, “Critical Issues in 157nm Lithography”. Journal of Vacuum Science and Technology B, 16-6, 3154-3157, 1998.

34. E. D. Palik, J. W. Gibson and R. T. Holm. “Internal-Reflection-Spectroscopy study of Adsorption of Water on $CaF_2$ Surfaces”. Surface Science 84, 164-178, 1979.

35. N. S. Nogar, E. C. Apel and R. C. Estler, “Mass Spectrometric Studies of Laser Damage in Calcium Fluoride”. NIST (U.S.) Special Publication 752, 42-48, 1987.

36. A. K. Green and E. Bauer. Journal of Applied Physics, 39, 2769, 1978.

37. P. A. Temple, D. L. Decker, T. M. Donovan and J. K. Bethke. NBS Special Publication 541, 37, 1978.

38. J. C. Zink, J. Reif and E. Matthias, “Water Adsorption on (111) Surfaces of BaF2 and CaF2”. Physical Review Letters, 68, 3595-3598, 1992.

39. S. D. Allen, J. O. Porteus, W. N. Faith and J. B. Franck, “Contaminant and Defect Analysis of Optical Surfaces by Infrared Laser Induced Desorption”. Applied Physics Letters, 45, 997-999, 1984.

40. H. K. Park, C. P. Grigoropoulos, W. P. Leung, A. C. Tam, “A Practical Excimer Laser-Based Cleaning Tool for Removal of Surface Contaminants”. IEEE Transactions on Components, Packaging, and Manufacturing Technology, Part A, 17, 631-643, 1994.

41. S. J. Lee, K. Imen and S. D. Allen, “Laser-Assisted Particle Removal from Silicon Surfaces”. Microelectronic Engineering, 20, 145-157, 1993.

42. J. O. Porteus, J. B. Franck, S. C. Seitel and S. D. Allen, “Defect Characteristics of Optical Surfaces using Pulsed Laser Damage Methods”. Optical Engineering, 25-10, 1171-1176, 1986.

43. J. O. Porteus, T. M. Donovan, J. L. Jernigan and W. N. Faith. NBS Special Publication, 541, 202, 1981.

44. S. C. Seital, J. O. Porteus, D. L. Decker, W. N. Faith and D. J. Grandjean. IEEE Journal of Quantum Electronics, QE-17, 2072- 2077, 1981.

45. S. M. Durbin, A. V. Deshmukh, T. D. Brooks and L. J. van de Burgt, “Precision Laser-based decontamination of microcavities”. Applied Surface Science, 129, 810-814, 1998.

46. O. Kreitschitzo, W. Husinsky, G. Betz and N. H. Tolk, “Laser Induced Desorption of Ions from Insulators Near the Ablation Threshold”. Nuclear Instruments & Methods in Physics Research Section B – Beam Interactions with Materials and Atoms, 78, 327-332, 1993.

47. O. Kreitschitz, W. Husinsky, G. Betz and N. H. Tolk, “Time-of-Flight Investigation of the Intensity Dependence of Laser-Desorbed Positive Ions from $SrF_2$”. Applied Physics A, 58, 563-571, 1994.

48. E. Matthias, S. Gogoll, E. Stenzel and M. Reichling, “ Laser-Stimulated Desorption from $CaF_2$ Crystals”. Radiation Effects and Defects in Solids, 128, 67-78, 1994.

49. M. Reichling, J. Sils, H. Johansen and E. Matthias, “Nanosecond UV Laser Damage and Ablation from Fluoride Crystals Polished by different techniques”. Applied Physics A – Materials Science & Processing, 69: S743-S747, Supplementary Source, 1999.

50. R. Bennewitz, M. Reichling and E. Matthias, “Force Microscopy of Cleaved and Electron-Irradiated $CaF_2$ (111) Surfaces in Ultra-High Vacuum”. Surface Science, 387, 69-77, 1997.

51. A.C. Tien, S. Backus, H. Kapteyn, M. Murnane, and G. Mourou, Phys. Rev. Lett. 82, 3883, 1999.

52. G. Vereecke, E. Rohr and M. M. Heyns, “Influence of beam incidence angle on dry laser cleaning of surface particles”. Applied Surface Science, 157, 67-73, 2000.

53. H. Johansen and G. Kastner. Journal Material Science, 33, 3839,1998.

54. Q. Qin, Z. Zhang, X. Yang and Q. Zheng, “Laser-Induced Desorption and Photofragmentation of Small Molecules Adsorbed on Surfaces”. SPIE volume 2547, 389 – 399.

# APPENDIX

Two C programs were developed to quicken the analysis process of the detected species from LID-TOFMS experiments. Program 1 sorts detected ion intensity values and mass values and displays result in an output file with two columns. The result file consists of detected ion intensity values and mass values arranged in descending and ascending orders respectively. The ion intensity series has ion intensity values and mass values as first and second columns. In the mass values series, mass values and ion intensity values are displayed in first and second columns respectively. The program allows a user to select the maximum number of ion intensities and mass values to be displayed.

Program 2 was used to obtain cumulative desorption fluence in threshold experiments or total desorption fluence in mapping experiments. This program was developed to work with the mass values of interest in this study. With a few modifications, it can be used to work with different mass values.

## Program 1

```
#include <stdio.h>
#include <string.h>
#include <stdlib.h>
#define MAX_ENTRIES 10000
#define A 4.9574
```

```
#define B 0.3105
#define FILENAME "outputresult"

void  sortionintensity (double * mass, double * ionint, int row_number, int sz, FILE * fp);
void  sortmass (double * mass, double * ionint, int row_number, int sz, FILE  * fp);

int main (int argc, char * argv[])
 {
    char filename[80];
    char tm_c[15];
    char ion_c[15];
    int i, k=0;
    int mul;
    int max;
    int maxplus;
    int row_number;
    double inp_mass [MAX_ENTRIES];
    double inp_ion [MAX_ENTRIES];
    double time;

    FILE * ifp = NULL;
    FILE * ofp = NULL;
    FILE * tfp = NULL;

    If (argc != 2)
     {
        printf ("Please provide the file name.\n");
        exit (1);
     }

     strcpy (filename,argv[1]);

     ofp = fopen (FILENAME,"w");
     if (ofp == NULL)
       {
         printf ("Could not create output file!\n");
         exit (1);
       }

     ifp = fopen (filename,"r");
```

```
if (ifp == NULL)
  {
    printf ("Wrong file!\n");
    exit (1);
  }

printf ("type mul equal to '-1000' for individual plot and '1000' for
average plot\n");
printf ("mul = ");
scanf ("%d", &mul);

i = 0;
while (!feof (ifp))
   {
     fscanf (ifp,"%s %s\n",tm_c,ion_c);
     time = atof (tm_c) * 1000000;
     inp_mass [i] = (((time - B)/A) * ((time - B)/A));
     inp_ion [i] = atof (ion_c) * mul;
     i++;
   }

printf ("enter the row number you want to start with\n");
printf ("row_number = ");
scanf ("%d", &row_number);
printf ("enter the maximum number of peaks you want to display\n");
printf ("max = ");
scanf ("%d", &max);
maxplus= row_number + max;
printf ("************ FOLLOWING ARE ION INTENSITIES GREATER THAN     1mV
IN DESCENDING ORDER\n");
sortionintensity (inp_mass,inp_ion, row_number, MAX_ENTRIES, ofp);
printf ("************ FOLLOWING ARE MASS REQUESTED IN ASCENDING
ORDER\n");
sortmass (inp_mass,inp_ion, row_number, MAX_ENTRIES, ofp);

tfp = fopen (FILENAME,"r");
while (!feof (tfp))
   {
      fscanf (tfp,"%s %s\n",inp_mass,inp_ion);
      k++;
```

```
       }

    if (k ==1)
      {
        fprintf(ofp,"NO MASS FOUND WTIH > 1mV\n");
        printf("NO MASS FOUND WTIH ION INTENSITY GREATER THAN
        1mV\n");
      }

   fclose(ifp);
   fclose(ofp);
   fclose(tfp);


   return 0;
 }


void  sortionintensity (double * mass, double * ionint, int st, int sz, FILE * fp)
 {
    int i, j;
    double temp1, temp2;
    fprintf (fp,"FOLLOWING ARE ION INTENSITIES GREATER THAN 1mV IN
    DESCENDING ORDER\n");

    for (i = st; i < sz; ++i)
         {
           for (j = i; j < sz; ++j)
                {
                   if ( ionint[j] > ionint[i])
                     {
                        temp1 = ionint[j];
                        temp2 = mass[j];
                        ionint[j] = ionint[i];
                        mass[j] = mass[i];
                        ionint[i] = temp1;
                        mass[i] = temp2;
                     }
                }
          }
```

```
    for (i = st; i < 1600; ++i)
         {
           if (ionint[i] >= 1)
             {
               if (ionint[i] <=200)
                 {
                   if ( mass[i] >= 1)
                     {
                        fprintf(fp,"%f %f\n",mass[i],ionint[i]);
                        printf("%f %f\n",mass[i],ionint[i]);
                        fflush(0);
                     }
                 }
             }
         }

    return;
  }


void  sortmass(double * mass, double * ionint, int st,  int sz, FILE * fp)
 {
   int i, j;
   double temp1, temp2;
   FILE * ifp2 = NULL;
   fprintf(fp,"FOLLOWING ARE MASS REQUESTED IN ASCENDING  ORDER\n");
   for (i = st; i < sz; ++i)
        {
          for (j = i; j < sz; ++j)
               {
                  if( mass[j] < mass[i])
                    {
                       temp1 = mass[j];
                       temp2 = ionint[j];
                       mass[j] = mass[i];
                       ionint[j] = ionint[i];
                       mass[i] = temp1;
                       ionint[i] = temp2;
                    }
```

```
              }
          }

    for (i = st; i < sz; ++i)
          {
            if (ionint[i] >= 1)
              {
                if (mass[i] >= 12 && mass[i]<=12.5)
                  {
                     if (mass[i] <=200)
                       {
                          fprintf(fp,"%f %f\n",mass[i],ionint[i]);
                          printf("%f %f\n",mass[i],ionint[i]);
                          fflush(0);
                       }
                  }
              }
          }

     return;
  }
```

## Program 2

```
#include <stdio.h>
#include <string.h>
#include <stdlib.h>
#define MAX_ENTRIES 20000
#define A 4.9574
#define B 0.3105
#define FILENAME "outputresult"

void  sortmass (double * mass, double * ionint, int row_number, int sz, double *);
double range [13][2] = { {11.8, 12.2}, {12.8,13.2}, {13.8,14.2}, {14.8,15.2}, {15.8,16.2},
{16.8,17.2}, {17.8,18.3}, {23.8,24.4}, {24.8,25.4}, {25.8,26.4}, {26.8,27.4}, {27.8,28.4},
{28.8,29.4} };
```

```
int main (int argc, char * argv[])
 {
    char filename [80];
    char outfilename [80];
    char tm_c [15];
    char ion_c [15];
    int i,m,n,k=0,count;
    char end [2];
    int mul, row_number;
    double inp_mass [MAX_ENTRIES];
    double inp_ion [MAX_ENTRIES];
    double time;
    double resultMass [30];

    FILE * ifp = NULL;
    FILE * ofp = NULL;
    FILE * tfp = NULL;

    for ( m=1;m<=1;m++)
        {
          itoa (m,outfilename,10);
          strcat (outfilename,"slides.out");
          ofp = fopen (outfilename,"w");

          for (count= 0;count<=12;count++)/*number of ranges*/
                    resultMass[count]=0;
              if (ofp == NULL)
                {
                  printf ("Could not create output file!\n");
                  exit (1);
                }
              mul = -1000;
              row_number = 1530;

              for ( n=1;n<=10;n++)
                  {
                    itoa (m,filename,10);
                    strcat (filename,"slides-");
                    itoa (n,end,10);
                    strcat (filename,end);
```

```
                     strcat (filename,".txt");
                     printf ("file name is : %s \n",filename);

                    ifp = fopen (filename,"r");
                    if (ifp == NULL)
                      {
                         printf("Wrong file!\n");
                         exit(1);
                      }

                    i = 0;
                    while (!feof(ifp))
                           {
                              fscanf(ifp,"%s %s\n",tm_c,ion_c);
                              time = atof(tm_c) * 1000000;
                              inp_mass[i] = (((time - B)/A) * ((time - B)/A));
                              inp_ion[i] = atof(ion_c) * mul;
                              i++;
                            }
                     sortmass (inp_mass,inp_ion,row_number,MAX_ENTRIES,
                     resultMass);

                    fclose(ifp);


                  }

             for ( count= 0;count<=12;count++)
                 fprintf(ofp,"%f %f\n",range[count][0],resultMass[count]);
                 fclose(ofp);
        }

    return 0;
 }


void  sortmass(double * mass, double * ionint, int st,  int sz,  double *resultMass)
  {
    int i,j;
    int k, cnt;
```

```
    FILE * ifp2 = NULL;
    double temp1, temp2;
    for (i = st; i < sz; ++i)
        {
            for (j = i; j < sz; ++j)
                {
                    if ( ionint[j] > ionint[i])
                      {
                          temp1 = mass[j];
                          temp2 = ionint[j];
                          mass[j] = mass[i];
                          ionint[j] = ionint[i];
                          mass[i] = temp1;
                          ionint[i] = temp2;
                      }
                }
        }

    for ( k= 0;k<=12;k++) /*k is same as count*/
        {
            cnt = 0;
            for (i = st; i < sz; ++i)
                {
                    if (ionint[i] >= 1)
                      {
                          if (mass[i] <= range[k][1] && mass[i] >= range[k][0])
                            {
                                resultMass[k] = resultMass[k] + ionint[i];
                                cnt = cnt +1;
                                if (cnt == 1)
                                break;
                                fflush(0);
                            }
                      }
                }
        }

    return;
}
```